A few things about the glacial history of the Transantarctic Mountains inferred from cosmogenic ^{26}Al, ^{10}Be, and ^{21}Ne concentrations in bedrock surfaces

Greg Balco,[1*] John O.H. Stone[2], Maciej Sliwinski[2], Claire Todd[3]

[1]Berkeley Geochronology Center, 2455 Ridge Road, Berkeley CA 94709 USA
[2]Earth and Space Sciences, University of Washington, Seattle WA 98195 USA
[3]Geosciences, Pacific Lutheran University, Tacoma WA 98447 USA

*To whom correspondence should be addressed. E-mail: *balcs@bgc.org*

Abstract

We measured concentrations of cosmogenic ^{26}Al, ^{10}Be, and ^{21}Ne in quartz from bedrock surfaces in the Transantarctic Mountains where stratigraphic and geomorphic evidence shows that the surfaces were covered by ice in the past, but were not glacially eroded during periods of ice cover. We explore to what extent we can use this information to learn about past glacier change. First, cosmogenic-nuclide concentrations in sandstone bedrock surfaces at two sites in the McMurdo Dry Valleys near 77°S are most easily explained by a scenario in which: i) sites more than ~100 m above the present ice surface are almost never ice-covered and erode steadily at 0.5-1.5 m Ma^{-1}, and ii) sites near the present ice margin experience similar erosion rates when ice-free, but have been covered by cold-based glacier ice as much as half the time during the past several million years. Nuclide concentrations in granite bedrock at a site in the Quartz Hills near 85°S, on the other hand, have not reached production-erosion equilibrium. Results from these sites are most easily explained by 4-6 Ma exposure at extremely low erosion rates of 5-10 cm Ma^{-1} with only very short periods of ice cover.

1 Introduction

In this paper we describe measurements of the cosmic-ray-produced radionuclides ^{26}Al, ^{10}Be, and ^{21}Ne from intermittently-glaciated bedrock surfaces in the Transantarctic Mountains. These bedrock surfaces are characteristic of much of the landscape of the Transantarctic Mountains in that geomorphic and stratigraphic evidence shows that they were covered by ice in the past, but the bedrock surfaces themselves lack any evidence of glacial modification and display only features associated with subaerial weathering and granular disintegration (e.g., Sugden et al.,

1999; Sugden and Denton, 2004; Sugden et al., 2005). As this relationship implies a polar climate cold enough to sustain only frozen-based and non-erosive glaciers, the geomorphology of these surfaces provides potential constraints on Cenozoic Antarctic climate and ice sheet change (Sugden et al., 1999; Sugden and Denton, 2004).

The goal of this paper is to attempt to quantify some of these constraints via cosmogenic-nuclide measurements. Concentrations of cosmic-ray-produced nuclides in rock surfaces reflect a balance between nuclide production during exposure of the surface to cosmic rays, loss of nuclide-enriched surface material due to erosion, and, for radionuclides, loss by radioactive decay. The relative importance of these processes varies according to the half-life of the nuclide in question, so comparing inventories of different nuclides can help to reconstruct the exposure history of the surface. For example, ^{26}Al and ^{10}Be are produced by cosmic-ray bombardment of quartz at a fixed ratio of ^{26}Al:^{10}Be = 6.75, but ^{26}Al decays twice as fast as ^{10}Be. Thus, if a quartz sample experiences a single period of surface exposure, ^{26}Al and ^{10}Be concentrations are uniquely related to the exposure time by their production ratio and decay constants. If this period of exposure is interrupted by periods during which the sample is shielded from the cosmic-ray flux, ^{26}Al inventory will decay faster than ^{10}Be during these periods, so the ^{26}Al/^{10}Be ratio will no longer conform to this relationship. Thus, disequilibrium between ^{26}Al and ^{10}Be concentrations can be used to identify surfaces that have experienced complex exposure histories.

This idea is important for our purposes here because many bedrock surfaces in glaciated regions show such disequilibrium (e.g., Bierman et al., 1999; Sugden et al., 2005). Many of the measurements that showed this were originally intended to determine the time these surfaces were exposed by ice retreat during the most recent deglaciation. However, the observations that i) nuclide concentrations were much higher (in some cases by orders of magnitude) than could have accumulated since ice retreat, and ii) ^{26}Al and ^{10}Be concentrations were not in equilibrium with continuous surface exposure, showed that these surfaces had not experienced significant subglacial erosion, and their cosmogenic-nuclide concentrations recorded the integrated effect of not one but many periods of exposure and ice cover. These surfaces are not useful for dating the most recent ice retreat, but on the other hand can potentially be used to learn about ice sheet history and surface weathering rates over many glacial-interglacial cycles.

In this paper we compile measurements of the cosmic-ray-produced nuclides ^{26}Al ($t_{1/2}$ =0.7 Ma), ^{10}Be ($t_{1/2}$ =1.4 Ma), and ^{21}Ne (stable) in quartz from surfaces that have these characteristics: they display both geomorphic evidence and cosmogenic-nuclide concentrations diagnostic of preservation under repeated episodes of cover by frozen-based ice. All the sites have nuclide concentrations that require an exposure history extending over many glacial-interglacial cycles, and many sites also show disequilibrium among concentrations of various nuclides. We explore to what extent we can use this information to learn about the history of the East Antarctic Ice Sheet over the past several million years.

2 Field sites

We describe observations from three sites: two sites, Mt. DeWitt and East Groin, in the McMurdo Dry Valleys in Victoria Land near 77° S; and one at the Quartz Hills in the southern Transantarctic Mountains near 86° S (Figure 1). At all these sites, glacial drift stratigraphically overlying the bedrock surfaces show that, at some time in the past, all or nearly all of the sample locations were covered by ice.

Mt. DeWitt is a nunatak on the westernmost edge of the Dry Valleys, directly adjacent to the polar plateau of the East Antarctic Ice Sheet (Figure 2). We collected bedrock samples between 1880 m and the summit at 2090 m. The bedrock surface consists of weathered carbonaceous sandstone of the Triassic Lashly Formation. Clasts of Ferrar dolerite, a dark mafic intrusive rock that occurs throughout the Dry Valleys, litter the surface (Figure 3). As this lithology does not outcrop on Mt. DeWitt itself, these clasts must be glacially transported. Above 1900 m, the frequency of dolerite erratics decreases notably, and erratics are sparse between 1900-2040 m. The only erratic we found above 2040 m was an isolated clast directly at the summit. As the summit of Mt. DeWitt was occupied for extended periods by researchers occupying positioning transponders during the Taylor Dome ice coring project, it is possible that this erratic was not naturally present at the summit. Thus, Mt. DeWitt was ice-covered at some time in the past to at least 2040 m elevation, but evidence that the summit was ever covered is weak.

East Groin is a sandstone buttress adjacent to lower Taylor Glacier (Figures 4, 5). We collected samples between the modern ice margin at 1380 m and the highest point accessible on

foot at 1720 m. The bedrock is quartzite sandstone of the Devonian Altar Mountain and Arena Formations. Dolerite clasts, although present at all elevations, are not necessarily diagnostic of ice cover at this site, because Ferrar dolerite outcrops above our sample sites. Thus, dolerite clasts at lower elevations could conceivably have been emplaced by rockfall, although the convex form of the buttress makes it unlikely that this process would lead to the observed widespread, sparse, and approximately uniform distribution of dolerite clasts. However, large quartzite cobbles derived from conglomerate facies of Beacon group sandstones, which we did not observe in place at this site, do indicate transport by ice. In addition, moraines of Taylor Glacier at Arena Valley, directly across the Taylor Glacier from the site, show that the Taylor Glacier was at least 500 m thicker than present at least once in the past several million years (Brook and Kurz, 1993). Thus, the majority of our sample sites, and most likely all of them, must have been covered by expanded Taylor Glacier ice at least once in the past.

The Quartz Hills are a mountainous ice-free area adjacent to Reedy Glacier. Benches and valleys in the Quartz Hills are covered by extensive glacial deposits ranging in age from Holocene to Pliocene or older (Mercer, 1968; Bromley et al., 2010). We collected granite bedrock samples between 1400 m, near the present ice surface elevation, and 1675 m along a ridge overlooking the confluence of Reedy and Colorado Glaciers on the west side of the "Quartz Hills bench" (Bromley et al., 2010) (Figures 6, 7). The toe of the ridge is covered by Last Glacial Maximum (LGM) aged glacial drift deposited 14-17 ka (Todd et al., 2010), and the lowest sample (03-RDY-096-QZH; 1400 m elevation) was collected from a rock buttress projecting from this drift 10 m below its upper limit. A thin scatter of cobbles associated with the older Reedy B drift, which is believed to have been emplaced during marine isotope stage 6 at 140-160 ka (Bromley et al., 2010), extends to $\sim$1460 m elevation, 10 m above the second-lowest sample (03-RDY-095-QZH; 1448 m elevation). No erratics occur on the bedrock ridge above this drift, but the remainder of our samples lie below the mapped upper limit of Reedy D and E drifts ($>$ 3.5 Ma and $>$ 4.5 Ma, respectively; Bromley et al., 2010) on the adjacent bench, so must have been ice-covered when these drifts were emplaced.

Despite evidence for ice cover, bedrock surfaces at all sites show no signs of subglacial erosion. Striations, polish, streamlining, plucking, or any other features characteristic of glacial erosion are absent. In contrast, all sites show surface features characteristic of extended weath-

ering under ice-free conditions, including weathering rinds, granular disintegration, frost-shattering, weathering pits, and fragile, cavernous forms (Figures 3, 4, 5, 7). Thus, geomorphic observations indicate that these bedrock surfaces have been subject to slow subaerial weathering during ice-free periods, but not to subglacial erosion during periods of ice cover. As we will show later, cosmogenic-nuclide concentrations are consistent with this conclusion.

3 Analytical methods

We isolated quartz from crushed rock samples by repeated etching in dilute HF, extracted Be and Al using standard methods of HF dissolution and column chromatography at the Cosmogenic Nuclide Lab at the University of Washington (Stone, 2004), measured total Al concentrations by ICP optical emission spectrophotometry of an aliquot of the dissolved quartz-HF solution, and measured Be and Al isotope ratios by accelerator mass spectrometry at both the Center for Accelerator Mass Spectrometry, Lawrence Livermore National Laboratory (LLNL-CAMS; Quartz Hills samples) and the Purdue Rare Isotope Measurement Laboratory (PRIME Lab; Mt. Dewitt and East Groin samples). ^{26}Al and ^{10}Be concentrations appear in Table 1. We used commercial Be ICP standards as ^{9}Be carrier. For samples measured at PRIME, full carrier and process blanks had 277000 $\pm$ 77000 atoms ^{10}Be, in all cases less than 0.5% of the total number of ^{10}Be atoms in the sample, and 230,000 $\pm$ 93000 atoms ^{26}Al, in all cases less than 0.2% of the total number of atoms in the sample. For samples measured at LLNL-CAMS, full carrier and process blanks had 66000 $\pm$ 28000 atoms ^{10}Be, in all cases less than 0.3% of the total number of atoms in the sample, and 65000 $\pm$ 40000 atoms ^{26}Al, in all cases less than 0.2% of the total number of atoms in the sample.

We extracted Ne from aliquots of the same HF-etched quartz samples in the Noble Gas Thermochronometry Lab of the Berkeley Geochronology Center by encapsulating the sample in a Ta packet and heating it under vacuum with a 75W, 810 nm diode laser. We analysed the released Ne on a MAP-215 mass spectrometer using a method that employs a ^{39}Ar spike to correct for isobaric interferences on masses 20 and 22. Balco and Shuster (2009b) give complete details of the measurement technique. Ne isotope ratios in all heating steps were were consistent with two-component mixing between atmospheric and cosmogenic Ne, that is, they were

not distinguishable at 95% confidence from the atmospheric-cosmogenic mixing line (Niedermann et al., 1993). However, quartz from Beacon group sandstones in the Dry Valleys is known to contain nucleogenic ^{21}Ne produced by the reaction ^{18}O(α,n)^{21}Ne as a result of U and Th decay. Both Middleton et al. (2012) and Balco et al. (2011) found, at different sites, that quartz in Beacon Group sandstones contained 7.7×10^6 atoms g^{-1} nucleogenic ^{21}Ne. Given the (high) ^{21}Ne concentrations and measurement precision for the samples in this study, this amount of nucleogenic ^{21}Ne is not sufficient to recognizably displace measured Ne isotope ratios from the atmospheric-cosmogenic mixing line. Thus, we calculate cosmogenic ^{21}Ne concentrations by i) first computing excess ^{21}Ne relative to atmospheric composition, and then ii) subtracting $7.7 \pm 2.4 \times 10^6$ atoms g^{-1} from this amount (the uncertainty estimate for the nucleogenic ^{21}Ne concentration is from Middleton et al. (2012)). The samples from the Quartz Hills are not Beacon Group sandstones, so it is unlikely that this is an accurate estimate of the nucleogenic ^{21}Ne concentration in these samples. However, this amount of nucleogenic ^{21}Ne would be at most 2.5% of the total excess ^{21}Ne concentration in any sample from the Quartz Hills. Thus, we accept even a large uncertainty in our estimate of nucleogenic ^{21}Ne for these samples as most likely negligible relative to measurement uncertainty. Summary ^{21}Ne concentrations appear in Table 1 and complete results of the step-degassing analyses in Table S1.

4 Production rates and decay constants.

We computed ^{10}Be production rates due to spallation using the global calibration data set and 'St' scaling scheme of Balco et al. (2008), then assumed that the spallogenic production ratios ^{26}Al/^{10}Be, ^{21}Ne/^{10}Be, and ^{21}Ne/^{26}Al are 6.75, 4.08, and 0.61, respectively (Balco and Shuster, 2009b). We used ^{26}Al and ^{10}Be decay constants of 9.83×10^{-7} and 4.99×10^{-7}, respectively (Nishiizumi, 2004; Chmeleff et al., 2009; Korschinek et al., 2009). Balco and Shuster (2009a) showed that this set of production ratios and decay constants, if not yet incontrovertibly correct, are at least internally consistent. We computed ^{26}Al and ^{10}Be production by muons using the method of Heisinger et al. (2002b,a) as implemented in Balco et al. (2008). ^{21}Ne production by muons has not been directly measured. However, Balco et al. (2011) found that cosmogenic ^{21}Ne concentrations in a deep sandstone core were consistent with muon interaction cross-

sections estimated by Fernandez-Mosquera et al. (2010). Thus, we adopt those cross-sections. It is important to note that because the samples in this study have very high concentrations of spallogenic ^{26}Al, ^{10}Be, and ^{21}Ne, concentrations of these nuclides due to muon production are small by comparison, and even large uncertainties in estimating production rates due to muons have a negligible effect on any of our conclusions.

5 Results and discussion

Table 1 summarizes ^{26}Al, ^{10}Be, and ^{21}Ne concentrations. Table 2 and Figure 8 represent these observations in two ways: as apparent exposure ages and apparent erosion rates as a function of elevation at each site. An 'apparent exposure age' is the exposure age calculated assuming a single period of continuous exposure at zero erosion, and an 'apparent erosion rate' is the surface erosion rate implied by the nuclide concentration given the assumption of continuous steady erosion for long enough that nuclide concentrations have reached equilibrium. In addition, Figures 9, 10, and 11 show normalized two-nuclide diagrams for the three nuclide pairs ^{26}Al-^{10}Be, ^{21}Ne-^{10}Be, and ^{21}Ne-^{26}Al.

5.1 Key features of the data

In this section we highlight three basic observations that are evident from Figures 8-11 and that highlight important differences in exposure history among our sample sites. In the next section we discuss what these observations tell us about the glacial and geomorphic history of the sample sites.

High-elevation samples at Dry Valleys sites are consistent with steady surface erosion and production-decay-erosion equilibrium. At higher-elevation sites at both Mt. Dewitt (above 1900 m) and East Groin (above 1400 m), apparent exposure ages vary among different nuclides, but apparent erosion rates are indistinguishable (Figure 8). In other words, concentrations of all three nuclides in these samples are not consistent with the hypothesis that these surfaces have experienced a single period of exposure at zero erosion, but they are consistent with the hypothesis that the surfaces have been eroding steadily for a long enough time that nuclide concentrations have reached an equilibrium between production and loss by radioactive decay and surface erosion. As evident from Figures 9, 10, and 11, this is equivalent to observing that these samples lie on

the steady erosion line with respect to all three nuclide pairs. Thus, the simplest explanation for these results is that these surfaces have been experiencing steady erosion at 0.5-1.5 m/Ma for a long time. How long a period of steady erosion is implied? The rate at which surface nuclide concentrations approach equilibrium with steady erosion depends on both the erosion rate and the decay constant of the nuclide in question. An effective half-life for equilibration with steady erosion is given by $-\ln(1/2)/(\lambda_i + \epsilon/\Lambda)$, where λ_i is the decay constant for nuclide i (a^{-1}), ϵ is the erosion rate (g cm^{-2} a^{-1}), and Λ is the effective attenuation length for spallogenic production (here taken to be 160 g cm^{-2}). These effective half-lives are 0.2-1 Ma for this range of erosion rates and nuclides, so 1-4 Ma would be required to reach 95% of the equilibrium value. Thus, there is no evidence that any of these sites were covered by ice during the past 1-4 Ma. We discuss how strong this constraint is later.

Low-elevation samples at Dry Valleys sites require periods of ice cover. At low-elevation sites at Mt. Dewitt (one site at 1878 m) and East Groin (four sites between 1314-1382 m), neither apparent exposure ages or apparent erosion rates are concordant among nuclides (Figure 8). In other words, nuclide concentrations are neither consistent with continuous surface exposure at zero erosion or with steady erosion. These samples lie outside the continuous exposure field on all three two-nuclide diagrams, in the region of intermittent exposure (Figures 9, 10, and 11). Thus, these sites have experienced at least one period of ice cover during their exposure history. In the next section we explore this observation further and try to learn about glacier history from these data.

High-elevation samples at the Quartz Hills display production-erosion equilibrium for ^{26}Al and ^{10}Be, but not for ^{21}Ne. At all sites in the Quartz Hills, apparent exposure ages differ significantly among all three nuclides, indicating that these sites have not experienced continuous surface exposure at zero erosion. However, apparent erosion rates derived from ^{26}Al and ^{10}Be are i) indistinguishable from each other, and ii) significantly different from the apparent ^{21}Ne erosion rate. This is most simply explained if these surfaces have been continuously exposed and subject to steady erosion for long enough that ^{26}Al and ^{10}Be concentrations have reached equilibrium with steady erosion, but ^{21}Ne concentrations have not. This is also evident on the two-nuclide diagrams: nuclide concentrations in these samples lie on the steady erosion line in the ^{26}Al-^{10}Be diagram, but lie between the simple exposure and steady erosion lines in ^{26}Al-

^{21}Ne and ^{10}Be-^{21}Ne diagrams. At the erosion rates implied by the ^{26}Al and ^{10}Be concentrations, ($\sim$ 0.1 m Ma^{-1}), the effective half-lives for ^{26}Al and ^{10}Be equilibration with steady erosion are 0.6 Ma and 1 Ma, respectively, so 3-4 Ma is required for ^{26}Al and ^{10}Be concentrations to become indistinguishable from erosional steady state. However, erosion rates of these surfaces are low enough that a significant fraction of loss of ^{26}Al and ^{10}Be from the surface is the result of radioactive decay, not erosion. Because ^{21}Ne is stable, the effective half-life for ^{21}Ne equilibration with steady erosion is 4 Ma, much longer than for ^{26}Al or ^{10}Be. Thus, $\sim$15-20 Ma would be required before ^{21}Ne concentrations were indistinguishable from production-erosion equilibrium. In other words, the ^{21}Ne concentrations retain a memory of the time these sites were first exposed, but ^{26}Al and ^{10}Be concentrations do not. If we assume a single period of continuous surface exposure at a steady erosion rate, with negligible production by muons, we can estimate both the exposure age and erosion rate of these samples by solving the (overdetermined) system of equations:

$$N_{26} = \frac{P_{26}}{\lambda_{26}+\frac{\epsilon}{\Lambda}}\left(1-\exp\left[-\left(\lambda_{26}+\frac{\epsilon}{\Lambda}\right)t\right]\right) \quad (1)$$

$$N_{10} = \frac{P_{10}}{\lambda_{10}+\frac{\epsilon}{\Lambda}}\left(1-\exp\left[-\left(\lambda_{10}+\frac{\epsilon}{\Lambda}\right)t\right]\right) \quad (2)$$

$$N_{21} = \frac{P_{26}\Lambda}{\epsilon}\left(1-\exp\left[-\left(\frac{\epsilon}{\Lambda}\right)t\right]\right) \quad (3)$$

for the erosion rate ϵ and the exposure time t, where N_i is the concentration (atoms g^{-1}) and P_i is the surface production rate (atoms g^{-1} a^{-1}) of nuclide i. Because, as described above, stratigraphic and geomorphic evidence shows that these sites were covered by ice one or more times, these assumptions imply that the duration of ice cover was short relative to the total duration of exposure; we discuss this more later.

We solved this system of equations for each sample using the nonlinear least squares algorithm in MATLAB, and estimated uncertainties via a 200-iteration Monte Carlo simulation. Figure 12 shows the results of this exercise. These results indicate that nuclide concentrations at all sites can be explained if these surfaces were originally exposed between 4-6 Ma, and have been eroding at 3-12 cm Ma^{-1} since that time. Surface exposure ages computed in this way are consistent with apparent exposure ages $>$ 4 Ma on boulders from Reedy E drift (Bromley et al., 2010), and thus with a scenario in which initial exposure of bedrock surfaces at this site was

coincident with emplacement of this drift.

The Monte Carlo uncertainty analysis shows that exposure ages computed in this way scatter somewhat more than expected from measurement uncertainty alone. This is most likely for two reasons: first, the assumption of continuous exposure at a steady erosion rate is oversimplified; a time-varying erosion rate or periods of cover by thick till could cause this assumption to fail. Second, we have disregarded stratigraphic evidence showing that these sites were, in fact, covered by ice for at least a short time. As noted by Mukhopadhyay et al. (2012) and others, one can easily construct exposure histories that include short periods of ice cover but yield nuclide concentrations that could also be the result of continuous surface exposure. The fact that ice cover is not required to explain the observed nuclide concentrations, however, shows that the duration of ice cover at these sites was short relative to their total exposure history. 'Short' in this context means thousands to tens of thousands of years – order 1-2% of the total exposure history. In addition, because of the geometric requirement that if higher-elevation sites are covered by ice then lower-elevation sites must also be covered, the fact that there is no relationship between exposure age or erosion rate computed in this way and site elevation is not consistent with a significant duration of ice cover as a source for the scatter in inferred exposure ages. To summarize, despite geomorphic evidence that all sites were covered by ice at least once in the past, the simplest explanation for the observed nuclide concentrations is that these surfaces were first exposed 4-6 Ma and have been eroding at 3-10 cm Ma^{-1}, with only short periods of ice cover, since that time.

Finally, it is worth noting that these are extraordinarily low erosion rates. In fact, disregarding ice cover in estimating exposure ages and erosion rates from Equations (1-3) causes us to overestimate erosion rates, so these are maximum limiting erosion rates under any assumptions.

5.2 Constraints on ice cover history

Samples that display nuclide concentrations out of equilibrium with continuous surface exposure at any erosion rate must have been covered by ice for a significant fraction of their history. Nuclide concentrations that are consistent with simple exposure, on the other hand, do not completely exclude any ice cover of the site in the past: as discussed above, if episodes of ice

cover were short relative to the total exposure history recorded by the nuclide inventory, nuclide concentrations would not be perturbed enough to be detectable. This must be the case in the data set here, because many samples are from sites where geological evidence requires ice cover at some time in the past, but have nuclide concentrations consistent with simple exposure. This includes samples between 1920 and 2040 m elevation at Mt. Dewitt, all samples from the Quartz Hills, and most likely samples above 1400 m at East Groin. For one thing, this is important because it highlights the fact that nuclide concentrations that show equilibrium with continuous surface exposure cannot be used to prove that sample sites were never covered by ice; a few thousand years of ice cover at the LGM, for example, would not detectably perturb ^{26}Al and ^{10}Be concentrations in bedrock surfaces that already had a long exposure history. In this section, we explore this issue further by addressing two questions: first, for the samples that have ^{26}Al, ^{10}Be, and ^{21}Ne concentrations consistent with simple exposure but geologic evidence for ice cover, what limits can be placed on the timing and duration of past ice cover? Second, for the samples that have nuclide concentrations requiring significant ice cover, what sort of ice cover histories are consistent with the nuclide concentrations? As discussed at length by Bierman et al. (1999) and many others subsequently, these questions do not have unique answers: because the nuclide concentrations reflect the total integrated exposure and burial of the surfaces, many ice cover histories that differ in the number, duration, and time of burial and exposure periods can yield the same nuclide concentrations. Thus, we will use the approach of proposing simple scenarios of ice sheet change and exploring under what conditions they are compatible with the observed nuclide concentrations.

Samples with geologic evidence of ice cover but nuclide concentrations consistent with continuous surface exposure. Samples between 1920 and 2040 m elevation at Mt. Dewitt, all samples from the Quartz Hills, and samples above 1400 m at East Groin have nuclide concentrations that can be explained by continuous surface exposure. However, geological evidence shows that these sites were covered by ice at some point. In this section, therefore, we ask how long these sites could have been covered by ice without causing nuclide concentrations to detectably diverge from equilibrium with continuous surface exposure. Because radioactive decay and surface erosion tend to efface evidence of past ice cover, the longer ago the period of burial, the longer the duration of burial can be and still satisfy this condition.

To explore this question, we will assume the following. First, the rock surface at a sample site has been steadily eroding at an erosion rate ϵ for long enough that nuclide concentrations have approximately reached equilibrium concentrations. At this point, nuclide concentrations are as follows:

$$N_{26,eq} = \frac{P_{26}}{\lambda_{26}+\frac{\epsilon}{\Lambda}} \quad (4)$$

$$N_{10,eq} = \frac{P_{10}}{\lambda_{10}+\frac{\epsilon}{\Lambda}} \quad (5)$$

$$N_{21,eq} = \frac{P_{21,sp}\Lambda}{\epsilon} + \frac{P_{21,\mu-}\Lambda_{\mu-}}{\epsilon} + \frac{P_{21,\mu fast}\Lambda_{\mu fast}}{\epsilon} \quad (6)$$

Although we consider only spallogenic production for ^{26}Al and ^{10}Be, we separately consider production by muons for ^{21}Ne. This is because at low erosion rates, muon-produced ^{10}Be and ^{26}Al produced at depth is mostly lost to radioactive decay by the time it gets to the surface, so ^{26}Al and ^{10}Be produced by muons is negligible by comparison with that due to spallation. This is not necessarily the case for a stable nuclide. See Balco and Shuster (2009b) for a very long discussion of this subject. Thus, $P_{21,sp}$, $P_{21,\mu-}$, and $P_{21,\mu fast}$ are surface production rates of ^{21}Ne by spallation, negative muon capture, and fast muon interactions, respectively. For this purpose we approximate the depth dependence of muon production by a simple exponential relationship and define $\Lambda_{\mu-}$ (1510 g cm^{-2}) and $\Lambda_{\mu fast}$ (4360 g cm^{-2}) to be effective attenuation lengths for negative muon capture and fast muon interactions (Heisinger et al., 2002b,a).

The sample is covered by ice at a time t_0 (years before present) and remains covered for a duration t_b (years). It is then exposed again and continues to erode at a rate ϵ until the present time. With these conditions the nuclide concentrations observed at the present time are:

$$N_{26} = N_{26,eq}e^{-\lambda_{26}t_0}e^{\frac{-\epsilon(t_0-t_b)}{\Lambda}} + \frac{P_{26}}{\lambda_{26}+\frac{\epsilon}{\Lambda}}\left[1-e^{-\left(\lambda_{26}+\frac{\epsilon}{\Lambda}\right)(t_0-t_b)}\right] \quad (7)$$

$$N_{10} = N_{10,eq}e^{-\lambda_{10}t_0}e^{\frac{-\epsilon(t_0-t_b)}{\Lambda}} + \frac{P_{10}}{\lambda_{10}+\frac{\epsilon}{\Lambda}}\left[1-e^{-\left(\lambda_{10}+\frac{\epsilon}{\Lambda}\right)(t_0-t_b)}\right] \quad (8)$$

$$N_{21} = N_{21,eq} \quad (9)$$

See Figure 13. We now assume that disequilibrium with continuous surface exposure would be detectable if the observed ratio of two nuclides was 3% lower than the equilibrium ratio and,

for a particular value of ϵ, ask what combinations of t_0 and t_b would satisfy this condition. For the ^{10}Be-^{21}Ne nuclide pair, for example, this is the same as specifying a value of ϵ and finding the set of (t_0, t_b) pairs that satisfy $N_{10}N_{21,eq}/N_{10,eq}N_{21} = 0.97$. This nuclide pair is the slowest to return to its production–decay-erosion equilibrium after a period of burial, so it gives the strongest constraints on the duration of past periods of ice cover.

Figure 13 shows the results of this exercise. First, it is important to note that a minimum of 60,000 years of continuous ice cover is required for the ^{10}Be/^{21}Ne ratio to decrease by 3% from the initial equilibrium ratio (the corresponding figure for ^{26}Al/^{10}Be and ^{26}Al/^{21}Ne is 30,000 years). Thus, a single period of ice cover shorter than this value would not be detectable under this criterion. Second, these results show that when the erosion rate is relatively high, e.g. 1 m Ma^{-1}, the observation of two-nuclide equilibrium is not very restrictive – only a relatively shorr time is required for nuclide concentrations to return to near-equilibrium values. For example, samples at higher elevations at Mt. DeWitt and East Groin, where concentrations of all three nuclides are in equilibrium with steady erosion, indicate surface erosion rates of 0.5-1.5 m Ma^{-1}. At these erosion rates, Figure 13 shows that the observation of equilibrium nuclide concentrations can exclude long periods of ice cover only in the past 1-2 Ma. Glacier thickening prior to that time would not be detectable. At the Quartz Hills, as discussed in the previous section, higher nuclide concentrations are best explained by lower erosion rates of 5-10 cm Ma^{-1}. Because erosion rates are lower, these sites can potentially record disequilibrium induced by long periods of ice cover for a much longer time; an episode of ice cover sustained for $\sim$0.1 Ma could potentially be detectable after $\sim$1 Ma. Thus, the Quartz Hills sites provide strong evidence that, despite clear geological evidence for occasional thickening of Reedy Glacier, glacier thickening was rare and short-lived during the Pleistocene.

Samples with nuclide concentrations inconsistent with simple exposure. Low-elevation samples at East Groin and Mt. DeWitt have nuclide concentrations that cannot be explained by continuous surface exposure and thus require episodes of ice cover. These samples have most likely experienced numerous periods of alternating surface exposure and burial beneath cold-based ice, such that the total duration of ice cover makes up a significant fraction of their total exposure history. For the East Groin sample sites, this is implied by moraines and glacial drift at many nearby sites adjacent to the Taylor Glacier that record glacier thickening and thinning,

most likely on a 100,000-year glacial-interglacial cycle (e.g., Brook and Kurz, 1993; Higgins et al., 2000). Presumably, such cyclical ice advances and retreats occurred during much of the Pleistocene and perhaps Pliocene. A straightforward way to evaluate whether a scenario of periodic, glacial-interglacial ice sheet change is consistent with our measurements is to hypothesize that surface nuclide concentrations have reached steady state such that nuclide production during ice-free periods is balanced by i) nuclide loss by radioactive decay, and ii) surface erosion during ice-free periods. Given this hypothesis as well as the assumptions that i) each glacial-interglacial cycle can be characterized by a constant cycle duration (t_c, here assumed to be 100,000 years) and a fraction of that period (f_b, dimensionless) during which the surface is ice-covered; and ii) there is no subglacial erosion, nuclide concentrations at the beginning of a glacial period are given by:

$$N_{26} = \frac{P_{26}}{\lambda_{26}+\frac{\epsilon}{\Lambda}} \frac{\left(1-\exp\left[-t_c(1-f_b)\left(\lambda_{26}+\frac{\epsilon}{\Lambda}\right)\right]\right)}{\left(1-\exp\left[-t_c\lambda_{26}\right]\exp\left[-\frac{\epsilon t_c(1-f_b)}{\Lambda}\right]\right)} \quad (10)$$

$$N_{10} = \frac{P_{10}}{\lambda_{10}+\frac{\epsilon}{\Lambda}} \frac{\left(1-\exp\left[-t_c(1-f_b)\left(\lambda_{10}+\frac{\epsilon}{\Lambda}\right)\right]\right)}{\left(1-\exp\left[-t_c\lambda_{10}\right]\exp\left[-\frac{\epsilon t_c(1-f_b)}{\Lambda}\right]\right)} \quad (11)$$

$$N_{21} = \frac{P_{21,sp}\Lambda}{\epsilon} + \frac{P_{21,\mu-}\Lambda_{\mu-}}{\epsilon} + \frac{P_{21,\mu fast}\Lambda_{\mu fast}}{\epsilon} \quad (12)$$

As discussed above, it is necessary to consider, at least approximately, production by muons for ^{21}Ne but not for the radionuclides. Note that we compute the equilibrium nuclide concentration for the beginning of a glacial period, to be consistent with the idea that Taylor Glacier thickens during interglacials (Higgins et al., 2000). For each pair of nuclides, one can solve the corresponding pairs of equations for values of the surface erosion rate during ice-free periods ϵ (g cm^2 a^{-1}) and the fraction of each glacial cycle spent covered by ice f_b. Of course, it would also be possible to search for values of these two parameters that best fit all three nuclide concentrations. However, as discussed below, that would discard some information about changes in the extent of glaciation over time that can potentially be gained by considering the nuclide pairs separately.

We solved Equations (10-12) for samples at Mt. Dewitt and East Groin using the nonlinear least squares algorithm in MATLAB, and used a linear error propagation approximation with numerical partial differentiation to estimate the uncertainties in inferred values of f_b at-

tributable to measurement uncertainty in nuclide concentrations.The results are shown in Figure 14. For samples whose nuclide concentrations are in equilibrium with continuous surface exposure – i.e., they plot in the region of continuous exposure on Figures 9, 10, and 11 – solving these equations must yield $f_b = 0$ within measurement uncertainty for all nuclide pairs. As discussed above, this is the case for all but the lowest sample at Mt. Dewitt and for samples above 1400 m at East Groin. If the scenario implied by Equations (10-12) is correct, f_b must be greater for samples at lower elevations, because the ice sheet cannot advance over higher sites without also covering the lower sites. This is the case at both Mt. Dewitt and East Groin. At Mt. Dewitt this calculation implies the lowest site is ice-covered for $\sim$20-40% of each glacial-interglacial cycle, but the adjacent site 50 m higher is almost never covered by ice. At East Groin, f_b values computed from each nuclide pair are similar among closely spaced samples, and, as expected, higher at lower elevation: the lowest two sites (near 1320 m) at East Groin are covered by ice for $\sim$50% of each cycle, and the two next highest sites (near 1390 m) are covered by ice $\sim$5-40% of the time. Thus, our observations are consistent with the hypothesis that the observed nuclide concentrations in low-elevation samples reflect an equilibrium between production during ice-free periods and loss by radioactive decay and surface erosion during interglaciations under a scenario of repeated, periodic glacial-interglacial cycles spanning the Pleistocene.

For the lowest four samples at East Groin and the lowest sample at Mt. Dewitt, values of f_b obtained by solving Equations (10-12) vary systematically among nuclide pairs: ^{26}Al-^{10}Be pairs imply higher values of f_b than ^{26}Al-^{21}Ne and ^{10}Be-^{21}Ne pairs. A likely explanation for this relies on the fact that nuclides with shorter half-lives reach equilibrium with a periodic exposure-burial history more rapidly. Thus, one possible explanation for the systematic offset among values of f_b inferred from the various nuclide pairs is that sites were, on average, more commonly covered by ice during the longer time period "remembered" by the ^{26}Al/^{21}Ne and ^{10}Be/^{21}Ne pairs than during the shorter time period recorded by the ^{26}Al-^{10}Be pair. That is, there has been an overall reduction in the frequency and/or duration of periods of ice cover in the past several million years. For example, the sample at 1314 m at East Groin has values of f_b of 0.67, 0.6, and 0.5 inferred from the ^{26}Al/^{10}Be, ^{26}Al/^{21}Ne, and ^{10}Be/^{21}Ne pairs, respectively. One can reproduce this result by assuming that i) the bedrock surface erodes at 0.5 m Myr^{-1} when it is ice free, and does not erode when it is ice-covered; ii) at 2.5 Ma, nuclide concentra-

tions had reached equilibrium (as defined by Equations 10-12) with repeated glacial-interglacial cycles consisting of 85,000 years of ice cover followed by 15,000 years of exposure; and iii) between 2.5 Ma and the present, the relative duration of ice cover gradually decreased so that the most recent cycle consisted of 50,000 years of ice cover and 50,000 years of exposure. Although this is one of many possible ice cover scenarios that would explain these observations, the idea that we infer higher values of f_b from nuclide pairs that take longer to equilibrate is in general agreement with the idea that glacier extent in the Dry Valleys was more extensive in the Pliocene than at present. (Denton et al., 1993).

6 Conclusions

^{26}Al, ^{10}Be, and ^{21}Ne concentrations in sandstone bedrock surfaces at Dry Valleys sites are most easily explained by the following scenario. First, sites at high elevations are rarely covered by ice and have been steadily and slowly eroding, at rates of 0.5-1.5 m Ma^{-1}, for at least 1-4 Ma, that is, long enough to reach production-decay-erosion equilibrium. Second, sites within $\sim$100 m above the present ice surface elevation experience similar surface erosion rates when ice-free, but have been repeatedly covered by cold-based glacier ice during many glacial-interglacial cycles. Sites near the present-day margin of the Taylor Glacier are covered by ice about half the time. In addition, differences in the average frequency of ice cover inferred from nuclide pairs that reach equilibrium at different rates is consistent with a Pliocene-to-present reduction in the fraction of the time these sites are covered by ice. Apparent surface erosion rates of 0.5-1.5 m Ma^{-1}, which appear to reflect the relative erodibility of Beacon Group sandstones in the Dry Valleys region, imply that the cosmogenic-nuclide concentrations at these sites do not record events significantly predating the Pleistocene.

Nuclide concentrations in granite bedrock at the Quartz Hills, on the other hand, have not reached production-erosion equilibrium, and show that sites have been covered by ice for an insignificant fraction of their total exposure history. Results from these sites are most easily explained by 4-6 Ma exposure at erosion rates of 5-10 cm Ma^{-1}. It appears that Quartz Hills bedrock is drastically more resistant to surface erosion than Beacon Group sandstones, so preserves a longer record of exposure.

Acknowledgements

This work was supported by the National Science Foundation under grants OPP-0838958 (Balco), OPP-0443535 (Balco), OPP-0229314 (Stone), OPP-0636818 (Stone), and by the Ann and Gordon Getty Foundation. Jaakko Putkonen and Dan Morgan assisted with fieldwork and sample collection in the Dry Valleys. Brenda Hall, Gordon Bromley and Howard Conway assisted with fieldwork and mapping at Reedy Glacier. David Shuster and Tim Becker assisted with the ^{21}Ne measurements. Bob Finkel and Dylan Rood assisted with AMS measurements at LLNL-CAMS.

References

Balco, G., Shuster, D., 2009a. ^{26}Al - ^{10}Be - ^{21}Ne burial dating. Earth and Planetary Science Letters 286, 570–575.

Balco, G., Shuster, D., 2009b. Production rate of cosmogenic ^{21}Ne in quartz estimated from ^{10}Be, ^{26}Al, and ^{21}Ne concentrations in slowly eroding Antarctic bedrock surfaces. Earth and Planetary Science Letters 281, 48–58.

Balco, G., Shuster, D., Blard, P.-H., Zimmermann, L., Stone, J. O. H., 2011. Cosmogenic ^{21}Ne production systematics in quartz inferred from a 25-meter sandstone core. Mineralogical Magazine 75, 473.

Balco, G., Stone, J., Lifton, N., Dunai, T., 2008. A complete and easily accessible means of calculating surface exposure ages or erosion rates from ^{10}Be and ^{26}Al measurements. Quaternary Geochronology 3, 174–195.

Bierman, P., Marsella, K., Patterson, C., Davis, P., Caffee, M., 1999. Mid-Pleistocene cosmogenic minimum age limits for pre-Wisconsinan glacial surfaces in southwestern Minnesota and southern Baffin Island; a multiple-nuclide approach. Geomorphology 27, 25–39.

Bromley, G., Hall, B., Stone, J. O., Conway, H., Todd, C., 2010. Late Cenozoic deposits at Reedy Glacier, Transantarctic Mountains: implications for former thickness of the West Antarctic Ice Sheet. Quaternary Science Reviews 29, 384–398.

Brook, E., Kurz, M., 1993. Surface-exposure chronology using in situ cosmogenic ^{3}He in Antarctic quartz sandstone boulders. Quaternary Research 39, 1–10.

Chmeleff, J., von Blanckenburg, F., Kossert, K., Jakob, D., 2009. Determination of the ^{10}Be half-life by multi-collector ICP mass spectrometry and liquid scintillation counting. Geochmica et Cosmochimica Acta 73, Supplement 1 (2009 Goldschmidt Conference), A221.

Denton, G., Sugden, D., Marchant, D., Hall, B., Wilch, T., 1993. East Antarctic ice sheet sensitivity to Pliocene climate change from a Dry Valleys perspective. Geografiska Annaler 75, 4.

Fernandez-Mosquera, D., Hahm, D., Marti, K., 2010. Calculated rates of cosmic ray muon-produced Ne in subsurface quartz. Geophysical Research Letters 37, 2010GL044106.

Granger, D., 2006. A review of burial dating methods using ^{26}Al and ^{10}Be. In: Siame, L., Bourlès, D., Brown, E. (Eds.), In-situ-produced cosmogenic nuclides and quantification of geological processes: Geological Society of America Special Paper 415. Geological Society of America, pp. 1–16.

Heisinger, B., Lal, D., Jull, A. J. T., Kubik, P., Ivy-Ochs, S., Knie, K., Nolte, E., 2002a. Production of selected cosmogenic radionuclides by muons: 2. Capture of negative muons. Earth and Planetary Science Letters 200 (3-4), 357–369.

Heisinger, B., Lal, D., Jull, A. J. T., Kubik, P., Ivy-Ochs, S., Neumaier, S., Knie, K., Lazarev, V., Nolte, E., 2002b. Production of selected cosmogenic radionuclides by muons 1. Fast muons. Earth and Planetary Science Letters 200 (3-4), 345–355.

Higgins, S., Hendy, C., Denton, G., 2000. Geochronology of Bonney Drift, Taylor Valley, Antarctica: evidence for interglacial expansions of Taylor Glacier. Geografiska Annaler: Series A, Physical Geography 82, 391–409.

Korschinek, G., Bergmaier, A., Dillmann, I., Faestermann, T., Gerstmann, U., Knie, K., von Gostomski, C., Maiti, M., Poutivtsev, M., Remmert, A., Rugel, G., Wallner, A., 2009. Determination of the ^{10}Be half-life by HI-ERD and liquid scintillation counting. Geochmica et Cosmochimica Acta 73, Supplement 1 (2009 Goldschmidt Conference), A685.

Liu, H., Jezek, B., Zhao, Z., 2001. Radarsat Antarctic Mapping Project digital elevation model, version 2. Tech. rep., National Snow and Ice Data Center, Boulder, CO, USA.

Mercer, J., 1968. Glacial geology of the Reedy Glacier area, Antarctica. Geological Society of America Bulletin 79, 471–486.

Middleton, J., Ackert, R., Mukhopadhyay, S., 2012. Pothole and channel formation in the McMurdo Dry Valleys of Antartica: new insights from cosmogenic nuclides. Earth and Planetary Science Letters 355-356, 341–350.

Mukhopadhyay, S., Ackert, R., Pope, A., Pollard, D., DeConto, R., 2012. Miocene to recent ice elevation variations from the interior of the West Antarctic Ice Sheet: constraints from geologic observations, cosmogenic nuclides and ice sheet modeling. Earth and Planetary Science Letters 337-338, 243–251.

Niedermann, S., Graf, T., Marti, K., 1993. Mass spectrometric identification of cosmic-ray-produced neon in terrestrial rocks with multiple neon components. Earth and Planetary Science Letters 118, 65–73.

Nishiizumi, K., 2004. Preparation of ^{26}Al AMS standards. Nuclear Instruments and Methods in Physics Research B 223-224, 388–392.

Stone, J., 2004. Extraction of Al and Be from quartz for isotopic analysis. UW Cosmogenic Nuclide Lab Methods and Procedures.
URL `http://depts.washington.edu/cosmolab/chem.html`

Sugden, D., Balco, G., Cowdery, S., Stone, J., Sass III, L., 2005. Selective glacial erosion and weathering zones in the coastal mountains of Marie Byrd Land, Antarctica. Geomorphology 67, 317–334.

Sugden, D., Denton, G., 2004. Cenozozic landscape evolution of the Convoy Range to Mackay Glacier area, Transantarctic Mountains: onshore to offshore synthesis. Geological Society of America Bulletin 116, 840–857.

Sugden, D., Summerfield, M., Denton, G., Wilch, T., McIntosh, W., Marchant, D., Rutford, R., 1999. Landscape development in the Royal Society Range, southern Victoria Land, Antarctica: stability since the mid-Miocene. Geomorphology 28, 181–200.

Todd, C., Stone, J., Conway, H., Hall, B., Bromley, G., 2010. Late Quaternary evolution of Reedy Glacier, Antarctica. Quaternary Science Reviews 29, 1328–1341.

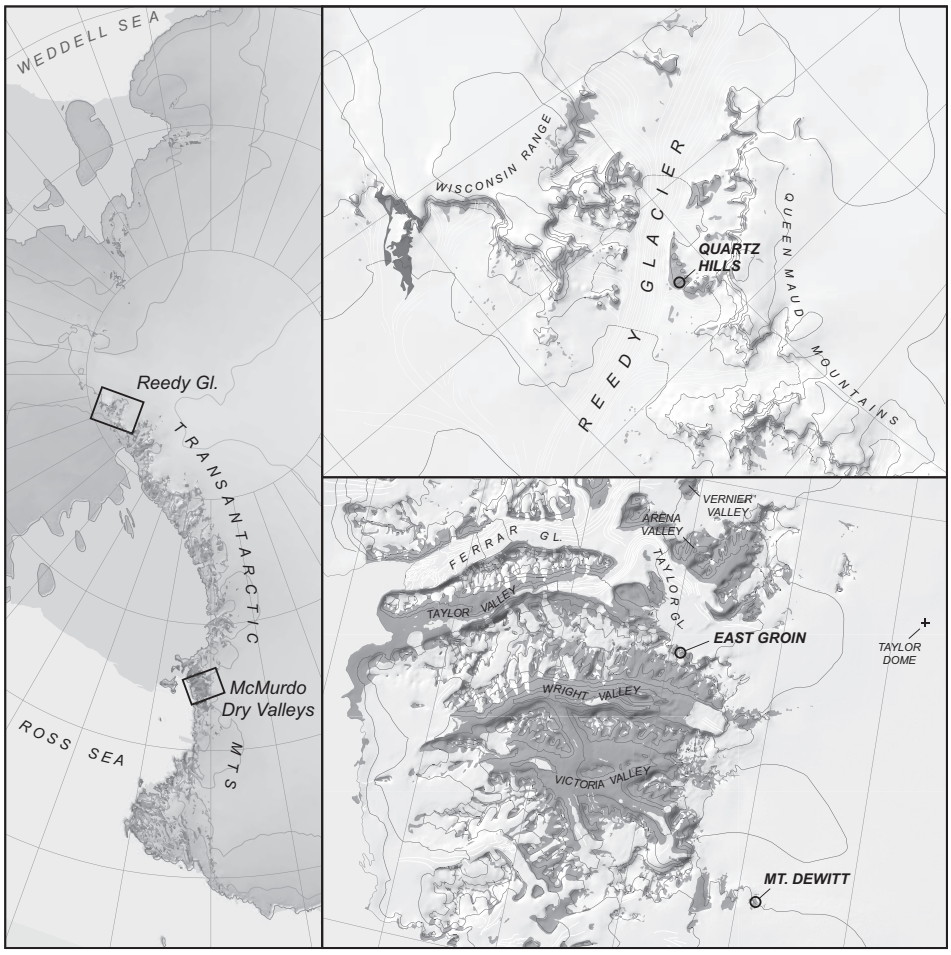

Figure 1: Site locations. Raster data on these maps is from the Antarctic Digital Database; shaded-relief topography is from the RAMP digital elevation model (Liu et al., 2001).

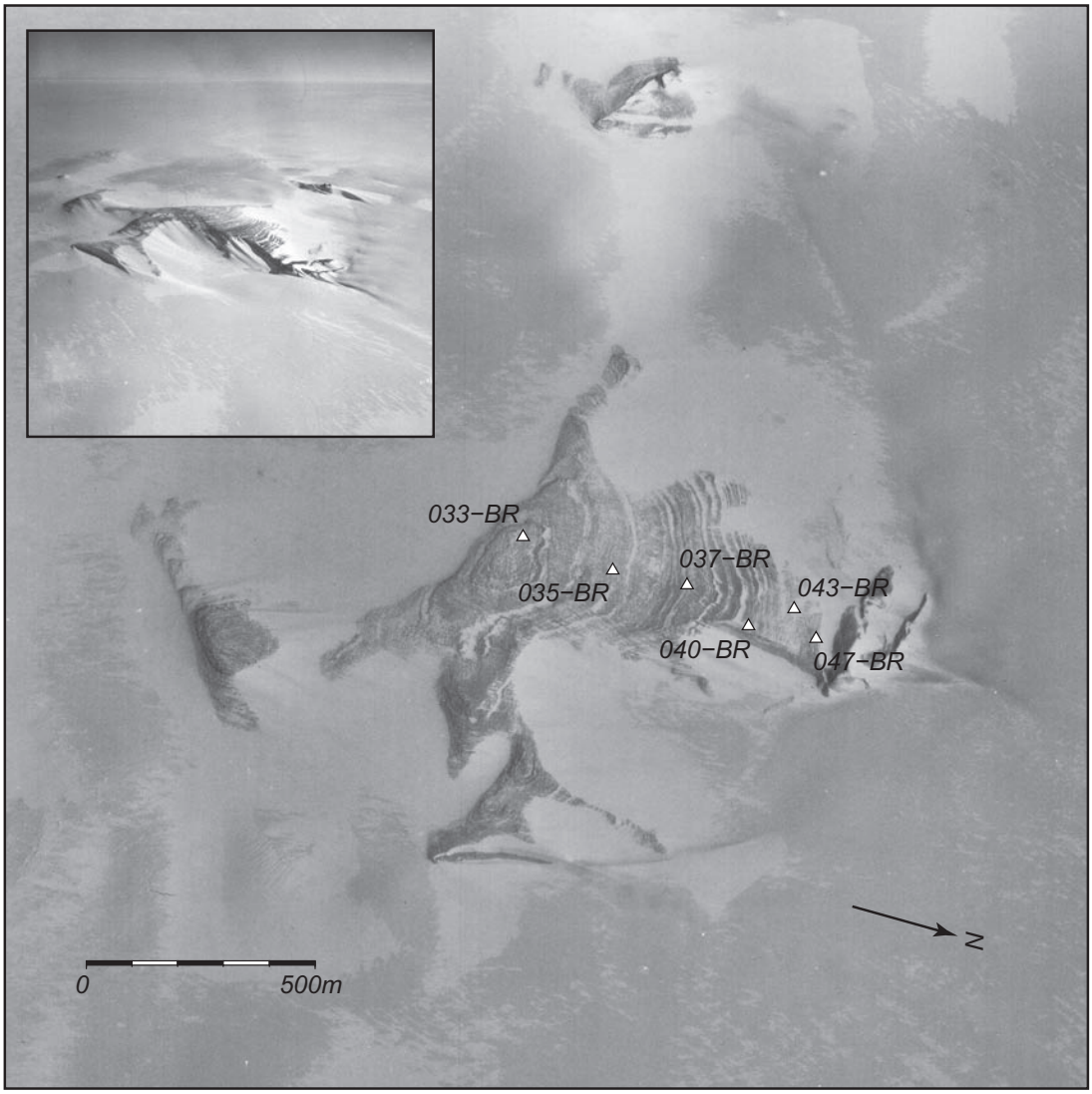

Figure 2: Overhead (U.S. Navy photo, line TMA2467, frame 21) and oblique (inset, line TMA279, frame 59) aerial photographs of Mt. DeWitt, showing sample locations.

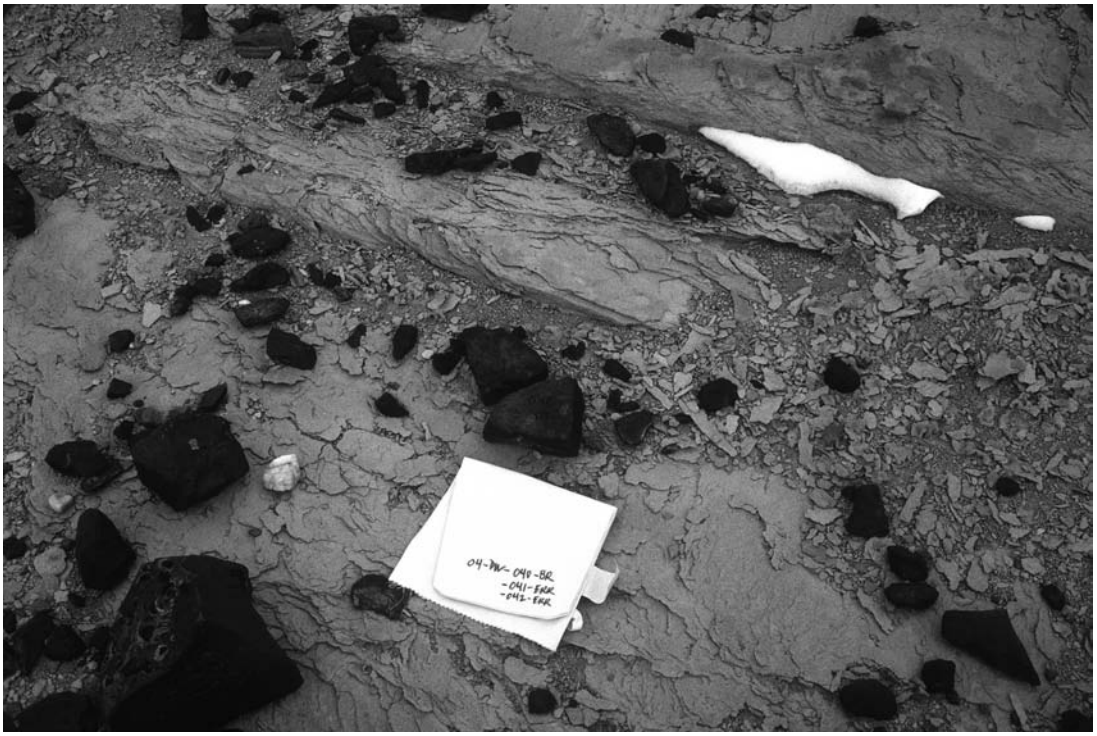

Figure 3: Photograph of representative sample site (04-DW-040-BR, 1948 m elevation) at Mt. DeWitt. Glacially transported clasts of Ferrar Dolerite overlie weathered sandstone bedrock displaying weathering rinds, granular disintegration, and loose surface clasts detached from the underlying bedrock.

Figure 4: Photograph of East Groin, looking SSE across the Taylor Glacier towards the Quartermain Mountains, including Arena and Beacon Valleys. The site of the uppermost sample (05-EG-118-BR, 1721 m) is in the foreground. Sandstone bedrock displaying weathering rinds as well as loose surface clasts detached from the underlying bedrock is overlain by a scatter of clasts of different lithology that were most likely glacially transported. Other sample sites are located along the crest of the sandstone ridge and at its toe near the glacier margin.

Figure 5: Photograph of the lowest sample site (05-EG-127-BR) at East Groin. Presumed glacial drift including clasts of Ferrar Dolerite overlie sandstone that displays weathering rinds as well as loose surface clasts detached from the underlying bedrock. View is up the Taylor Glacier to NW.

Figure 6: Overview of sample transect at the Quartz Hills, viewed from the medial moraine between Colorado and Reedy Glaciers. The sample transect approximately follows the right-hand skyline of the prominent ridge in the middle ground. The main Quartz Hills bench of Bromley et al. (2010) sits left of the ridge, at mid height in the photo. Light grey deposits covering the bench and running across the base of the ridge mark the limit of LGM ice cover. Darker deposits covering the ridge face left of the exposed bedrock are older Reedy B and Reedy D Drifts (Bromley et al., 2010). Ice responsible for deposition of Reedy D and Reedy E Drifts overtopped the bedrock spur.

Figure 7: Location of sample 03-RDY-096-QZH (1400 m), at the bottom of the Quartz Hills elevation transect. The modern ice margin is visible in the background. The bedrock surface displays a weathering rind in places, granular disintegration, and weathering pits. Glacially transported clasts in the potholes on the bedrock surface were emplaced at the LGM 14-17 ka.

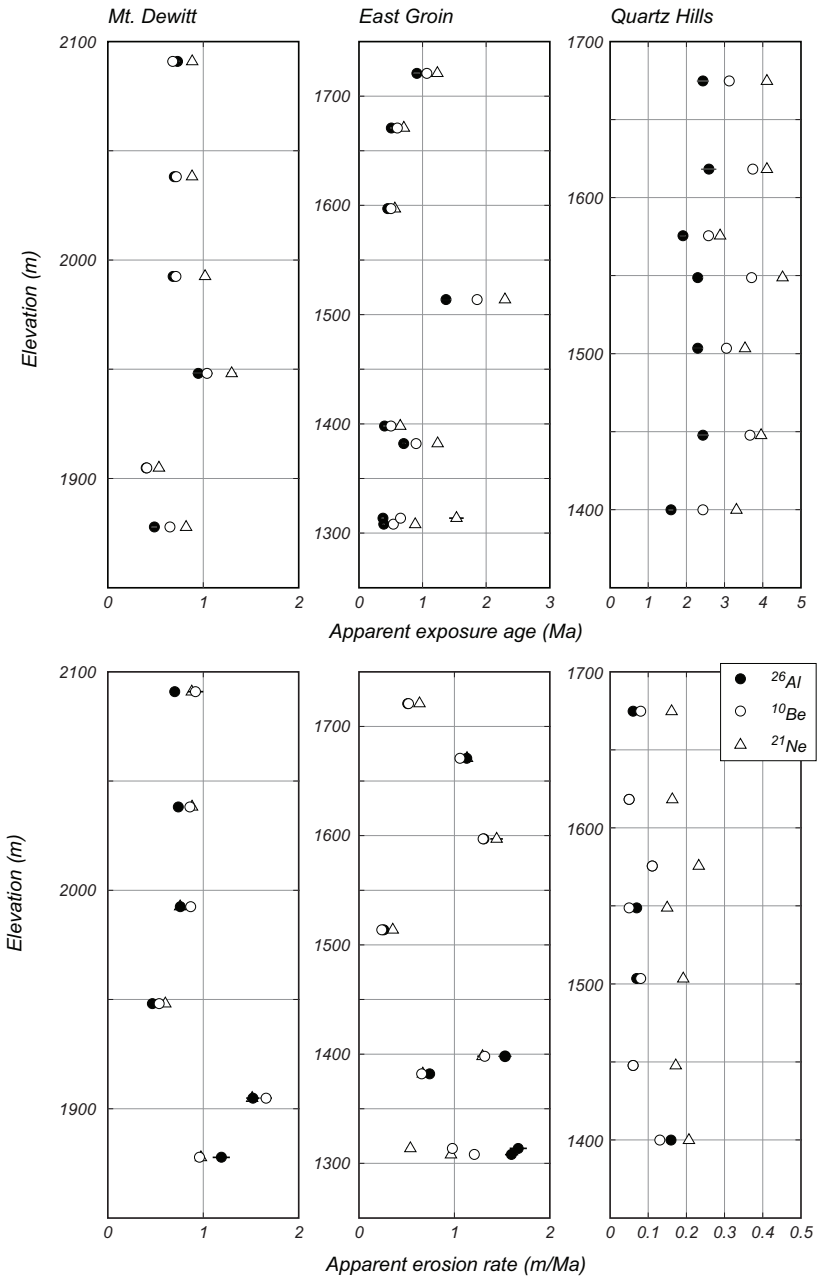

Figure 8: Apparent exposure age-elevation and apparent erosion rate-elevation relationships at Mt. DeWitt, East Groin, and the Quartz Hills. Error bars (1σ) reflect measurement uncertainty only and, where not visible, are smaller than the size of the symbols.

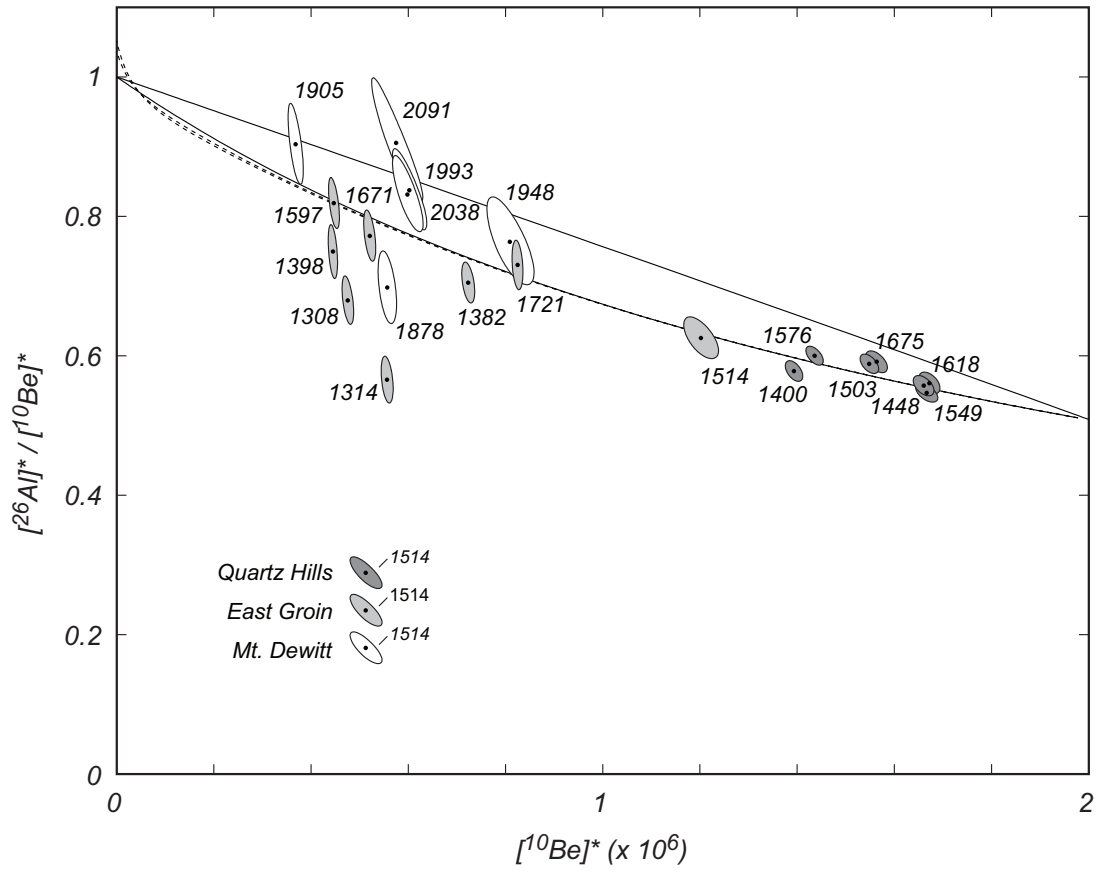

Figure 9: ^{26}Al - ^{10}Be two-nuclide diagram. See Granger (2006) for a complete discussion of this diagram. The solid black lines denote the so-called 'simple exposure region,' which is the region of the diagram where nuclide concentrations can lie given a single period of continuous surface exposure at any erosion rate. The upper boundary is the 'simple exposure line,' which denotes nuclide concentrations permissible given continuous surface exposure and zero erosion; the lower boundary is the 'steady erosion line,' which denotes nuclide concentrations expected if a surface has eroded steadily for long enough to reach an equilibrium nuclide concentration. These lines are drawn using the production ratios and decay constants given in the text and include only spallogenic production. The dashed lines include production by muons, and are included to show that the effect of muon production is negligible compared to measurement uncertainty for samples with high apparent exposure ages such as we observe here. The superscripted star in the axis labels indicates that nuclide concentrations have been normalized to their respective surface production rates. Ellipses are 68% confidence regions reflecting measurement uncertainties only. They are labeled with the sample elevations.

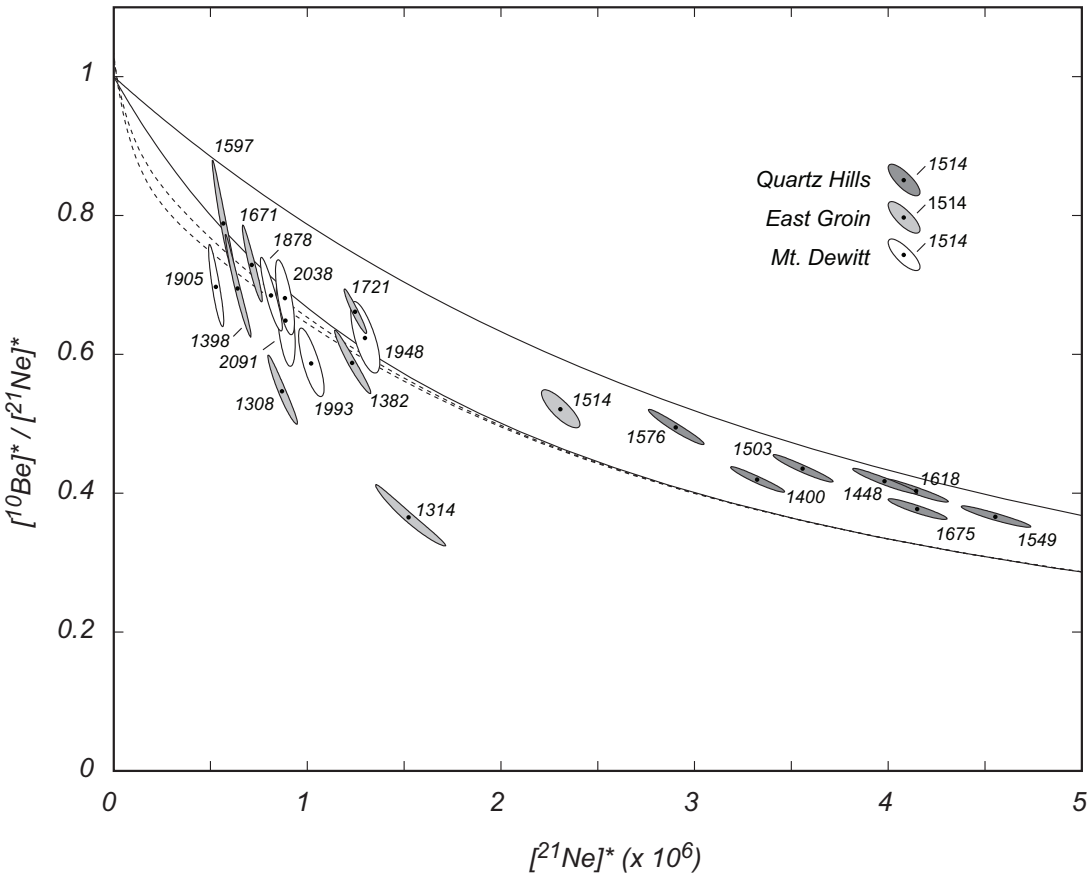

Figure 10: ^{10}Be - ^{21}Ne two-nuclide diagram. The construction of the diagram and the symbols used are as described in the caption to Figure 9.

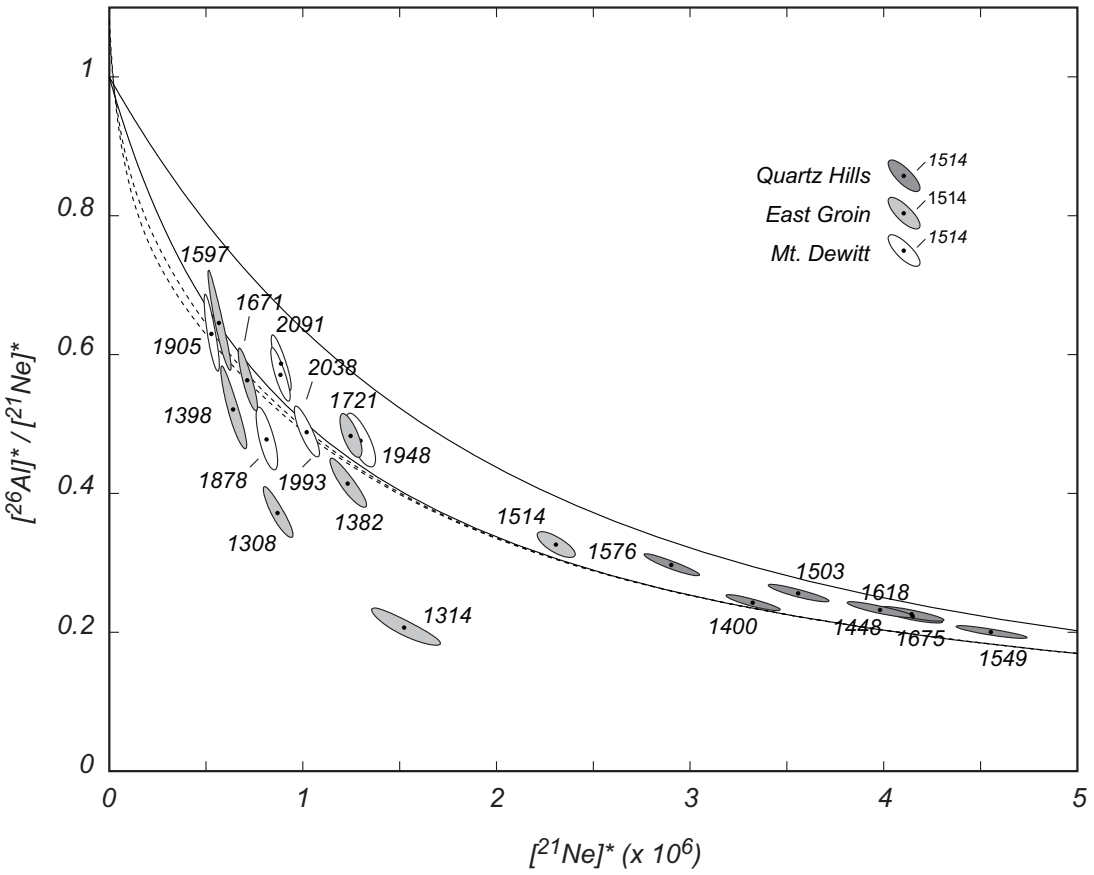

Figure 11: ^{26}Al - ^{21}Ne two-nuclide diagram. The construction of the diagram and the symbols used are as described in the caption to Figure 9.

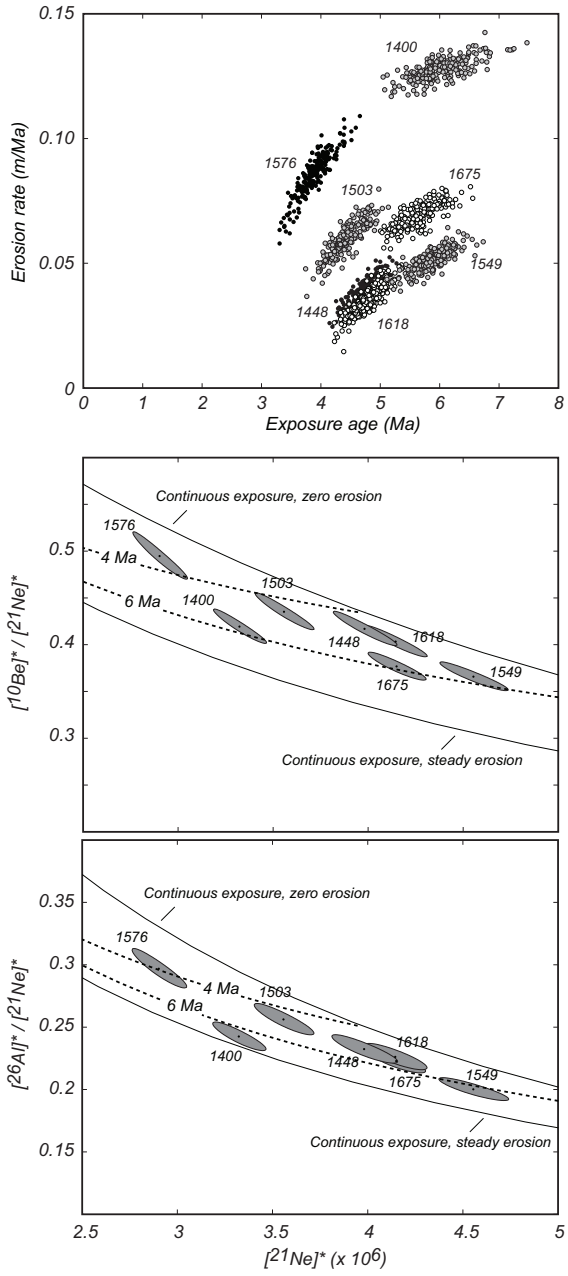

Figure 12: Upper panel, exposure ages and erosion rates calculated by solving the system of equations (1-3) for samples at the Quartz Hills. The dots are the result of a 500-point Monte Carlo simulation including measurement uncertainty only. The middle and lower panels show sections of ^{26}Al-^{21}Ne and ^{10}Be-^{21}Ne two nuclide diagrams from Figures 10 and 11, respectively, with isolines for 4 and 6 Ma exposure duration (at a range of erosion rates) added to the continuous exposure region. This provides similar information as the upper pane by showing that all the data are consistent within measurement uncertainty with this range of exposure ages.

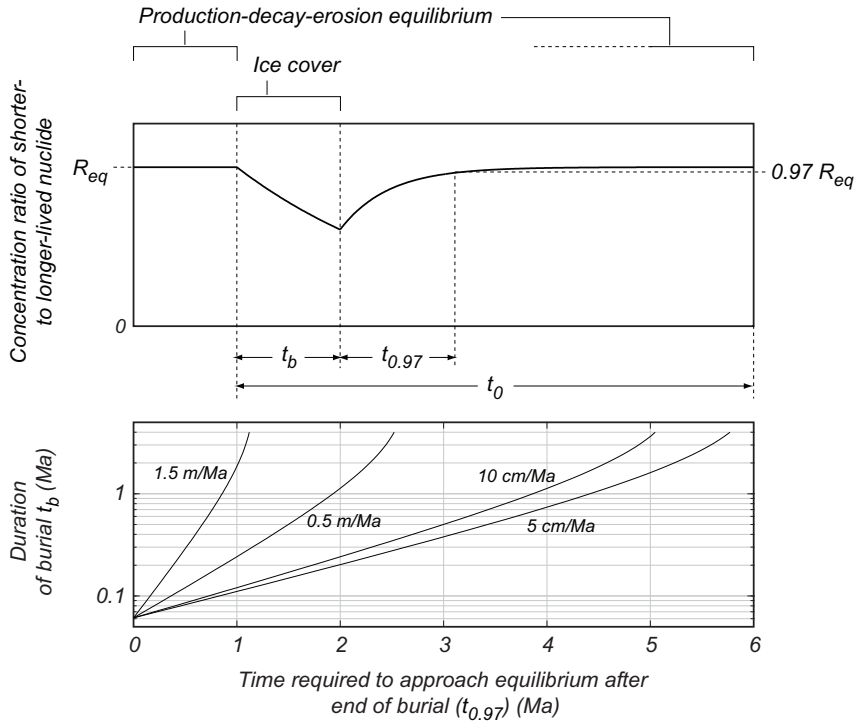

Figure 13: An attempt to answer the question, 'if a nuclide pair displays equilibrium with steady erosion at present, what constraint does that observation place on the timing and duration of past periods of ice cover?' The upper panel shows the scenario envisioned in Equations 4-9: the ratio of two nuclides (here shown as the ratio of the shorter- to longer-lived nuclide) begins at a value in equilibrium with steady erosion. When the sample is buried and erosion ceases, the ratio diverges from the equilibrium ratio due to radioactive decay. When it is uncovered again and erosion resumes, the ratio recovers to the equilibrium ratio at a rate that depends on the erosion rate and the half-lives of the nuclides in question. The length of time $t_{0.97}$ is how long it takes to reach a point where it is indistinguishable from (specifically, 97% of) the equilibrium ratio. The lower panel shows the constraints implied by this scenario on the timing and duration of burial of a sample that is observed to have a ^{10}Be/^{21}Ne ratio indistinguishable (specifically, within 3% of) the equilibrium ratio for a given erosion rate. For example, a sample exhibiting ^{10}Be - ^{21}Ne concentrations in equilibrium with 0.5 m Ma^{-1} erosion means that a period of ice cover ending 2 Ma can have been no longer than 1 Ma. When erosion rates are relatively high (1.5 m Ma^{-1}) constraints on past ice cover are relatively weak: for example, it only takes ca. 1 Ma for the ^{10}Be/^{21}Ne system to forget about any duration of past burial. Sites with lower erosion rates provide stronger constraints.

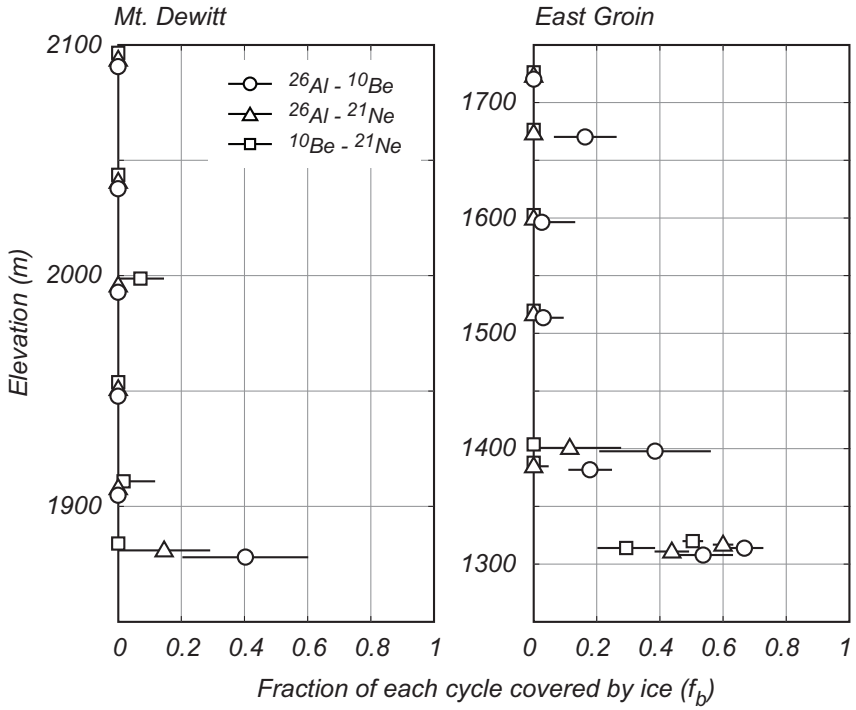

Figure 14: Variation with elevation of the fraction f_b of each glacial cycle during which each sample site is covered by ice inferred by solving the relevant pairs of Equations (4-6), for sites at Mt. Dewitt and East Groin. The results from different nuclide pairs from the same sample have been slightly displaced vertically to improve readability. The error bars reflect 68% confidence intervals given measurement uncertainty only and are estimated by numerical partial differentiation and adding in quadrature. Where ice cover is never permitted by a particular nuclide pair for a particular sample, no error bar is shown.

Table 1. Site information and cosmogenic-nuclide concentrations.

Sample name	Latitude (DD)	Longitude (DD)	Elevation (m)	Thickness (cm)	Density (g cm^{-2})	Topographic shielding	[^{10}Be][1] (10^6 atoms g^{-1})	[^{26}Al][2] (10^6 atoms g^{-1})	Excess [^{21}Ne][3] (10^6 atoms g^{-1})	Cosmogenic [^{21}Ne][4] (10^6 atoms g^{-1})	No. of ^{21}Ne analyses[5]
Mt. Dewitt sandstone bedrock											
04-DW-033-BR	-77.2046	159.8414	2091	3	2.2	1.000	19.7 ± 1.2	120.5 ± 3.0	130.8 ± 4.2	123.1 ± 4.8	2
04-DW-035-BR	-77.2012	159.8422	2038	2	2.2	0.999	19.95 ± 0.79	113.1 ± 2.8	126.6 ± 3.9	118.9 ± 4.6	2
04-DW-037-BR	-77.1987	159.8415	1993	3.5	2.2	0.999	18.99 ± 0.68	106.9 ± 2.8	139.0 ± 5.1	131.3 ± 5.6	2
04-DW-040-BR	-77.1962	159.8436	1948	2.5	2.2	0.999	25.0 ± 1.0	129.5 ± 5.0	170.8 ± 6.1	163.1 ± 6.6	1
04-DW-043-BR	-77.1949	159.8410	1905	4	2.2	0.998	10.91 ± 0.31	66.7 ± 2.2	71.2 ± 2.1	63.5 ± 3.2	3
04-DW-047-BR	-77.1939	159.8430	1878	6	2.2	0.998	15.95 ± 0.37	75.4 ± 3.4	102.2 ± 3.7	94.5 ± 4.4	2
East Groin sandstone bedrock											
05-EG-118-BR	-77.6419	160.9399	1721	7	2.2	0.982	20.56 ± 0.20	101.7 ± 3.3	133.8 ± 3.2	126.1 ± 4.0	2
05-EG-119-BR	-77.6442	160.9446	1671	7	2.2	0.998	12.69 ± 0.20	66.4 ± 1.8	78.3 ± 2.4	70.6 ± 3.4	3
05-EG-120-BR	-77.6534	160.9511	1597	2.5	2.2	1.000	10.65 ± 0.19	59.1 ± 1.5	62.5 ± 3.1	54.8 ± 4.0	1
05-EG-122-BR	-77.6611	160.9420	1514	2.5	2.2	0.999	26.85 ± 0.55	113.8 ± 2.9	216.7 ± 5.5	209.0 ± 6.0	1
05-EG-123-BR	-77.6720	160.9639	1308	2.5	2.2	0.998	9.00 ± 0.15	41.4 ± 1.2	74.4 ± 3.2	66.7 ± 4.0	3
05-EG-124-BR	-77.6720	160.9639	1314	10	2.2	0.998	10.03 ± 0.15	38.5 ± 1.5	119.0 ± 8.4	111.3 ± 8.7	2
05-EG-126-BR	-77.6649	160.9468	1398	4	2.2	0.991	8.89 ± 0.13	45.2 ± 1.5	59.6 ± 2.8	51.9 ± 3.7	2
05-EG-127-BR	-77.6650	160.9392	1382	7	2.2	0.996	14.04 ± 0.18	67.1 ± 1.7	104.6 ± 4.4	96.9 ± 5.0	2
Quartz Hills bedrock											
03-RDY-090-QZH	85.9050	-132.8025	1675	2	2.7	1.000	39.57 ± 0.40	158.5 ± 2.5	434 ± 10	426 ± 11	1
03-RDY-091-QZH	85.9037	-132.8106	1618	2	2.7	0.959	38.90 ± 0.34	147.8 ± 2.5	399 ± 10	391 ± 10	1
03-RDY-092-QZH	85.9032	-132.8129	1576	2	2.7	0.932	31.43 ± 0.28	127.8 ± 1.7	265.3 ± 8.2	257.6 ± 8.5	1
03-RDY-093-QZH	85.9029	-132.8144	1549	2	2.7	0.945	36.21 ± 0.35	134.2 ± 2.0	409 ± 11	401 ± 11	1
03-RDY-094-QZH	85.9022	-132.8194	1503	2	2.7	0.927	31.87 ± 0.28	127.1 ± 1.8	304.5 ± 8.5	296.8 ± 8.8	1
03-RDY-095-QZH	85.9022	-132.8501	1448	2	2.7	0.945	33.32 ± 0.29	125.8 ± 1.9	331.6 ± 9.0	323.9 ± 9.4	1
03-RDY-096-QZH	85.9003	-132.8376	1400	2	2.7	0.930	26.49 ± 0.23	103.8 ± 1.5	263.7 ± 7.0	256.0 ± 7.4	1

[1]Normalized to the Be isotope ratio standards of Nishiizumi et al. (2007)
[2]Normalized to the Al isotope ratio standards of Nishiizumi (2004)
[3]Excess ^{21}Ne is ^{21}Ne not accounted for by trapped Ne of atmospheric isotope composition and includes both cosmogenic and nucleogenic ^{21}Ne.
[4]Cosmogenic ^{21}Ne concentration reflects subtraction of estimated nucleogenic ^{21}Ne concentration from measured excess ^{21}Ne concentration. See text for details.
[5]Complete results of step-heating Ne analyses appear in Table S1.

Table 2. Apparent exposure ages and erosion rates inferred from ^{26}Al, ^{10}Be, and ^{21}Ne concentrations individually.

	Apparent exposure ages (Ma)									Apparent erosion rates (m/Myr)								
Sample name	From ^{10}Be	Internal uncertainty	External uncertainty	From ^{26}Al	Internal uncertainty	External uncertainty	From ^{21}Ne	Internal uncertainty	External uncertainty	From ^{10}Be	Internal uncertainty	External uncertainty	From ^{26}Al	Internal uncertainty	External uncertainty	From ^{21}Ne	Internal uncertainty	External uncertainty
Mt. Dewitt bedrock																		
04-DW-033-BR	0.68	0.05	0.09	0.73	0.03	0.10	0.88	0.03	0.09	0.92	0.08	0.14	0.70	0.04	0.13	0.90	0.04	0.08
04-DW-035-BR	0.72	0.03	0.08	0.70	0.03	0.09	0.88	0.03	0.09	0.86	0.05	0.12	0.74	0.04	0.13	0.90	0.04	0.08
04-DW-037-BR	0.71	0.03	0.08	0.68	0.03	0.09	1.01	0.04	0.11	0.87	0.05	0.12	0.76	0.04	0.13	0.79	0.03	0.07
04-DW-040-BR	1.04	0.06	0.13	0.95	0.06	0.15	1.29	0.05	0.14	0.54	0.04	0.09	0.47	0.05	0.11	0.62	0.03	0.05
04-DW-043-BR	0.41	0.01	0.04	0.40	0.02	0.05	0.52	0.03	0.06	1.66	0.06	0.18	1.52	0.07	0.21	1.53	0.08	0.14
04-DW-047-BR	0.65	0.02	0.07	0.49	0.03	0.06	0.81	0.04	0.09	0.96	0.03	0.12	1.19	0.09	0.19	1.00	0.05	0.09
East Groin bedrock																		
05-EG-118-BR	1.07	0.01	0.12	0.91	0.05	0.14	1.24	0.04	0.13	0.52	0.01	0.08	0.51	0.04	0.11	0.66	0.02	0.05
05-EG-119-BR	0.60	0.01	0.06	0.51	0.02	0.06	0.71	0.03	0.08	1.06	0.02	0.12	1.13	0.05	0.17	1.15	0.06	0.10
05-EG-120-BR	0.51	0.01	0.05	0.45	0.01	0.05	0.56	0.04	0.07	1.30	0.03	0.15	1.31	0.05	0.18	1.45	0.11	0.15
05-EG-122-BR	1.86	0.06	0.28	1.37	0.07	0.26	2.29	0.07	0.24	0.24	0.01	0.05	0.26	0.03	0.09	0.36	0.01	0.03
05-EG-123-BR	0.54	0.01	0.06	0.39	0.01	0.04	0.86	0.05	0.10	1.21	0.03	0.14	1.60	0.07	0.21	0.97	0.06	0.09
05-EG-124-BR	0.65	0.01	0.07	0.38	0.02	0.04	1.51	0.12	0.19	0.98	0.02	0.12	1.67	0.09	0.22	0.56	0.04	0.06
05-EG-126-BR	0.50	0.01	0.05	0.40	0.02	0.05	0.63	0.04	0.08	1.32	0.03	0.15	1.53	0.07	0.21	1.31	0.10	0.14
05-EG-127-BR	0.90	0.01	0.10	0.70	0.03	0.09	1.22	0.06	0.14	0.66	0.01	0.09	0.74	0.04	0.13	0.69	0.04	0.06
Quatz Hills bedrock																		
03-RDY-090-QZH	3.12	0.08	0.67	2.43	0.16	0.89	4.12	0.10	0.42	0.080	0.005	0.030	0.060	0.010	0.060	0.161	0.004	0.013
03-RDY-091-QZH	3.74	0.10	0.98	2.59	0.20	1.05	4.12	0.11	0.43	0.050	0.005	0.030	0.050	0.010	0.060	0.162	0.004	0.013
03-RDY-092-QZH	2.58	0.05	0.47	1.91	0.07	0.49	2.88	0.10	0.30	0.110	0.007	0.040	0.110	0.010	0.060	0.234	0.008	0.019
03-RDY-093-QZH	3.71	0.11	0.96	2.30	0.13	0.77	4.52	0.12	0.47	0.050	0.005	0.030	0.070	0.010	0.060	0.149	0.004	0.012
03-RDY-094-QZH	3.05	0.06	0.64	2.30	0.13	0.77	3.53	0.10	0.37	0.080	0.005	0.030	0.070	0.010	0.060	0.192	0.006	0.015
03-RDY-095-QZH	3.67	0.09	0.94	2.43	0.15	0.89	3.95	0.11	0.41	0.060	0.005	0.030	0.060	0.010	0.060	0.172	0.005	0.014
03-RDY-096-QZH	2.43	0.04	0.42	1.60	0.06	0.34	3.30	0.09	0.34	0.130	0.007	0.040	0.160	0.010	0.060	0.208	0.006	0.017

Supplementary data for Balco and others, "A few things about the glacial history of the Transantactic Mountains inferred from cosmogenic ^{26}Al, ^{10}Be, and ^{21}Ne concentrations in bedrock surfaces."

Table S1: Complete results of step-degassing Ne measurements. "Excess" ^{21}Ne is defined as ^{21}Ne in excess of that attributable to trapped Ne with atmospheric isotope composition. It comprises predominantly cosmogenic ^{21}Ne and, to a lesser extent, nucleogenic ^{21}Ne produced as a result of U-series decay. As discussed in the text, we subtract an estimated nucleogenic ^{21}Ne concentration from these measurements of excess ^{21}Ne to yield an estimate of the cosmogenic ^{21}Ne concentration.

Sample name	Aliquot	Aliquot weight (g)	Heating temperature (deg C)	Heating time (hr)	Total ^{20}Ne released[1] (10^9 atoms)	Total ^{21}Ne released[2] (10^6 atoms)	^{21}Ne / ^{20}Ne[3] (10^{-3})	^{22}Ne / ^{20}Ne[3] (10^{-3})	Excess ^{21}Ne[4] This heating step (10^6 atoms g^{-1})	Excess ^{21}Ne as % of ^{21}Ne released in this heating step	Percent of total excess ^{21}Ne released in this step	Total excess ^{21}Ne (10^6 atoms g^{-1})
04-DW-033-BR	c	0.0576	1100	0.3	2.2228 +/- 0.0252	14.273 +/- 0.499	6.317 +/- 0.117	105.5 +/- 1.3	130.08 +/- 4.76	52	100.0	130.1 +/- 4.8
			1100	0.33	0.0849 +/- 0.0345	-0.143 +/- 0.096	-1.667 +/- 1.303	28.4 +/- 22.6	-			
	d	0.0499	1100	0.3	1.5811 +/- 0.0193	11.487 +/- 0.556	7.148 +/- 0.275	106.5 +/- 1.6	133.31 +/- 8.91	58	100.0	133.3 +/- 8.9
			1100	0.33	0.0192 +/- 0.0097	0.04 +/- 0.087	2.082 +/- 4.581	107.7 +/- 85	-			
04-DW-035-BR	a	0.0733	1100	0.3	2.4417 +/- 0.0476	16.708 +/- 0.686	6.74 +/- 0.118	106.8 +/- 1.3	126.39 +/- 4.64	55	100.0	126.4 +/- 4.6
			1100	0.33	0.0556 +/- 0.0088	0.263 +/- 0.111	4.665 +/- 2.096	84.6 +/- 29.5	-			
	b	0.0448	700	0.3	1.5746 +/- 0.0379	10.023 +/- 0.482	6.344 +/- 0.18	108.9 +/- 2.1	119.29 +/- 6.98	53	94.0	127.0 +/- 7.3
			1100	0.3	0.1026 +/- 0.0062	0.647 +/- 0.096	6.293 +/- 0.968	86 +/- 13.8	7.68 +/- 2.19	53	6.0	
04-DW-037-BR	a	0.0597	1100	0.3	3.8367 +/- 0.0748	20.152 +/- 0.848	5.173 +/- 0.102	102.8 +/- 0.9	142.8 +/- 7.13	42	100.0	142.8 +/- 7.1
			1100	0.3	0.0434 +/- 0.0052	0.034 +/- 0.077	0.783 +/- 1.762	49.1 +/- 32.6	-			
	b	0.0535	1100	0.3	1.6681 +/- 0.0348	12.295 +/- 0.589	7.268 +/- 0.215	106.9 +/- 1.5	134.96 +/- 7.29	59	100.0	135.0 +/- 7.3
			1100	0.33	-0.0314 +/- 0.0136	0.089 +/- 0.082	-2.788 +/- 2.853	2.9 +/- 41	-			
04-DW-040-BR	a	0.0679	1100	0.3	2.9319 +/- 0.057	20.307 +/- 0.839	6.82 +/- 0.116	105.6 +/- 1	167.27 +/- 5.97	56	97.9	170.8 +/- 6.1
			1100	0.33	0.0128 +/- 0.0091	0.279 +/- 0.092	21.469 +/- 16.779	164.1 +/- 153.7	3.56 +/- 1.41	87	2.1	
04-DW-043-BR	c	0.0615	1100	0.3	1.2044 +/- 0.0163	8.249 +/- 0.315	6.721 +/- 0.179	103.9 +/- 1.9	73.9 +/- 3.66	55	100.0	73.9 +/- 3.7
			1100	0.3	0.0719 +/- 0.0101	0.278 +/- 0.093	3.808 +/- 1.375	85.5 +/- 23.1	-			
	d	0.0649	1100	0.3	0.726 +/- 0.0115	6.869 +/- 0.281	9.31 +/- 0.282	105.6 +/- 2.6	71.32 +/- 3.36	67	100.0	71.3 +/- 3.4
			1100	0.33	0.0158 +/- 0.0094	-0.016 +/- 0.089	-0.991 +/- 5.587	55.3 +/- 89.5	-			
	e	0.0614	700	0.3	0.6564 +/- 0.0172	6.094 +/- 0.322	9.269 +/- 0.346	110 +/- 2.9	67.68 +/- 4.11	68	100.0	67.7 +/- 4.1
			1100	0.3	0.095 +/- 0.0076	0.303 +/- 0.082	3.192 +/- 0.886	92 +/- 16	-			
04-DW-047-BR	c	0.0585	1100	0.3	1.0356 +/- 0.0218	9.16 +/- 0.341	8.659 +/- 0.253	104.9 +/- 2.5	101.32 +/- 4.97	65	100.0	101.3 +/- 5.0
			1100	0.33	0.008 +/- 0.0108	0.092 +/- 0.084	11.315 +/- 18.479	331.1 +/- 479.4	-			
	d	0.0484	1100	0.3	0.6919 +/- 0.0125	7.173 +/- 0.318	10.162 +/- 0.371	104.1 +/- 2.5	103.38 +/- 5.65	70	100.0	103.4 +/- 5.7
			1100	0.33	0.0158 +/- 0.0103	0.088 +/- 0.087	5.433 +/- 6.41	104 +/- 106.6	-			
05-EG-118-BR	d	0.1506	400	0.3	0.8632 +/- 0.0179	17.707 +/- 0.74	20.654 +/- 0.712	119.8 +/- 3.1	101.82 +/- 4.61	87	75.0	135.8 +/- 5.2
			700	0.3	1.0929 +/- 0.0233	7.764 +/- 0.364	7.157 +/- 0.288	111.6 +/- 2.7	30.58 +/- 2.2	59	22.5	
			1100	0.3	0.1947 +/- 0.0122	1.083 +/- 0.111	5.603 +/- 0.65	108.6 +/- 9.1	3.38 +/- 0.78	47	2.5	
	e	0.1451	400	0.3	0.7413 +/- 0.0211	15.502 +/- 0.497	20.777 +/- 0.651	128.7 +/- 4.9	92.07 +/- 3.47	86	69.5	132.5 +/- 4.1
			700	0.3	1.1861 +/- 0.0226	9.172 +/- 0.339	7.708 +/- 0.223	108.5 +/- 2.7	38.97 +/- 1.98	62	29.4	
			1100	0.3	0.2227 +/- 0.0178	0.87 +/- 0.137	3.898 +/- 0.676	98 +/- 12.3	1.46 +/- 1.01	24	1.1	
05-EG-119-BR	g	0.0574	700	0.3	0.7712 +/- 0.0156	6.874 +/- 0.335	8.878 +/- 0.334	111.5 +/- 2.6	79.77 +/- 4.78	67	93.0	85.8 +/- 5.1
			1100	0.3	0.1008 +/- 0.0116	0.645 +/- 0.102	6.378 +/- 1.227	114.9 +/- 19.9	6.05 +/- 1.88	54	7.0	
	h	0.0495	700	0.3	0.5778 +/- 0.0134	5.462 +/- 0.275	9.421 +/- 0.392	118 +/- 3.7	75.71 +/- 4.92	69	100.0	75.7 +/- 4.9
			1100	0.3	0.0943 +/- 0.0171	0.086 +/- 0.122	0.911 +/- 1.298	113.5 +/- 25.4	-			
	l	0.1408	400	0.3	0.6224 +/- 0.0194	10.025 +/- 0.397	16.005 +/- 0.658	125.2 +/- 4.9	58.36 +/- 2.86	82	76.3	76.5 +/- 3.2
			750	0.3	1.1222 +/- 0.0266	5.887 +/- 0.219	5.23 +/- 0.169	104 +/- 3.5	18.17 +/- 1.42	43	23.7	
			1100	0.3	0.1661 +/- 0.0158	0.426 +/- 0.123	2.557 +/- 0.772	107.2 +/- 15.7	-			

05-EG-120-BR	d	0.1357	400	0.3	0.68 +/- 0.0244	8.249 +/- 0.317	12.057 +/- 0.527	113.2 +/- 4.9	46.15 +/- 2.4	76	73.8	62.5 +/- 3.1
			750	0.3	1.4793 +/- 0.0256	6.476 +/- 0.281	4.365 +/- 0.157	100.9 +/- 2	15.39 +/- 1.74	32	24.6	
			1100	0.3	0.1398 +/- 0.0173	0.544 +/- 0.133	3.879 +/- 1.055	104.8 +/- 19.2	0.96 +/- 1.05	24	1.5	
05-EG-122-BR	f	0.1327	400	0.3	0.3677 +/- 0.0208	22.021 +/- 0.636	59.516 +/- 3.357	167.9 +/- 11.3	158.38 +/- 4.84	95	73.1	216.7 +/- 5.5
			750	0.3	0.9865 +/- 0.0212	10.383 +/- 0.351	10.496 +/- 0.28	107.6 +/- 3	56.26 +/- 2.41	72	26.0	
			1100	0.3	0.1811 +/- 0.0135	0.806 +/- 0.137	4.439 +/- 0.817	108.2 +/- 13.1	2.04 +/- 1.08	34	0.9	
05-EG-123-BR	a	0.0528	1000	0.3	2.4131 +/- 0.0479	10.869 +/- 0.519	4.457 +/- 0.173	100.2 +/- 2	68.71 +/- 8.03	33	100.0	68.7 +/- 8.0
			1100	0.3	0.562 +/- 0.0139	1.618 +/- 0.12	2.85 +/- 0.2	98.6 +/- 3.7	-			
	b	0.0531	1000	0.3	1.9778 +/- 0.0264	10.12 +/- 0.404	5.064 +/- 0.124	103 +/- 1.5	78.74 +/- 4.74	41	100.0	78.7 +/- 4.7
			1100	0.3	0.0218 +/- 0.0126	0.152 +/- 0.089	6.935 +/- 5.689	225.3 +/- 145.8	-			
	c	0.0610	700	0.3	1.9856 +/- 0.0309	10.02 +/- 0.437	5.027 +/- 0.139	102.9 +/- 1.5	67.58 +/- 4.67	41	94.4	71.6 +/- 5.1
			1100	0.3	0.4565 +/- 0.0127	1.601 +/- 0.132	3.496 +/- 0.277	103.6 +/- 4.4	4.04 +/- 2.08	15	5.6	
05-EG-124-BR	c	0.0486	700	0.3	2.0333 +/- 0.0247	11.228 +/- 0.457	5.476 +/- 0.125	101.6 +/- 1.2	105.69 +/- 5.4	46	94.4	112.0 +/- 6.0
			1100	0.3	0.3606 +/- 0.0139	1.383 +/- 0.125	3.802 +/- 0.348	108.4 +/- 5.8	6.28 +/- 2.61	22	5.6	
	d	0.0656	700	0.3	2.2857 +/- 0.0267	14.597 +/- 0.573	6.333 +/- 0.126	100.6 +/- 1.2	118.03 +/- 4.61	53	95.3	123.9 +/- 5.0
			1100	0.3	0.5934 +/- 0.0169	2.154 +/- 0.139	3.6 +/- 0.219	103.2 +/- 4.5	5.82 +/- 2	18	4.7	
05-EG-126-BR	c	0.0678	700	0.3	0.757 +/- 0.0156	6.28 +/- 0.312	8.225 +/- 0.33	108.8 +/- 3.2	58.98 +/- 3.89	64	97.1	60.7 +/- 4.2
			1100	0.3	0.2577 +/- 0.0125	0.888 +/- 0.108	3.416 +/- 0.429	111.9 +/- 8.8	1.74 +/- 1.64	13	2.9	
	e	0.0682	700	0.3	0.6588 +/- 0.0146	5.758 +/- 0.275	8.71 +/- 0.33	111.4 +/- 3.6	55.73 +/- 3.43	66	94.9	58.7 +/- 3.7
			1100	0.3	0.0708 +/- 0.0095	0.411 +/- 0.092	5.796 +/- 1.502	145.1 +/- 27.1	2.97 +/- 1.42	49	5.1	
05-EG-127-BR	a	0.0445	1000	0.3	0.4924 +/- 0.0126	6.248 +/- 0.308	12.575 +/- 0.543	114.3 +/- 4.5	106.89 +/- 6.63	76	98.9	108.1 +/- 7.0
			1100	0.3	0.0301 +/- 0.0087	0.142 +/- 0.096	4.67 +/- 3.426	189.2 +/- 73.1	1.2 +/- 2.24	38	1.1	
	b	0.0613	1000	0.3	0.5589 +/- 0.0145	7.801 +/- 0.346	13.834 +/- 0.521	113.3 +/- 4.1	99.53 +/- 5.42	78	97.3	102.3 +/- 5.7
			1100	0.3	0.0304 +/- 0.0145	0.26 +/- 0.088	8.445 +/- 4.926	191.7 +/- 103.4	2.79 +/- 1.61	66	2.7	
05-EG-121-ERR	a	0.0516	700	0.3	1.605 +/- 0.0315	25.333 +/- 0.918	15.754 +/- 0.298	119.7 +/- 2	399.76 +/- 12.17	81	98.4	406.3 +/- 12.4
			1100	0.3	0.3008 +/- 0.0123	1.227 +/- 0.109	4.067 +/- 0.37	109.7 +/- 6.8	6.49 +/- 2.18	27	1.6	
	b	0.0428	700	0.3	1.4152 +/- 0.0235	20.229 +/- 0.782	14.254 +/- 0.303	117.4 +/- 1.9	375.3 +/- 11.84	79	99.3	377.8 +/- 12.1
			1100	0.3	0.1392 +/- 0.0105	0.517 +/- 0.091	3.705 +/- 0.694	121.3 +/- 12.9	2.48 +/- 2.25	21	0.7	
05-EG-125-ERR	a	0.0640	700	0.3	1.0643 +/- 0.0214	23.86 +/- 0.859	22.376 +/- 0.426	124.7 +/- 2.8	324.03 +/- 9.65	87	97.6	332.0 +/- 9.8
			1100	0.3	0.1794 +/- 0.0133	1.036 +/- 0.111	5.755 +/- 0.721	132.6 +/- 12.8	7.92 +/- 1.85	49	2.4	
	b	0.0578	700	0.3	1.0632 +/- 0.0217	21.567 +/- 0.821	20.229 +/- 0.473	121.9 +/- 2.5	318.95 +/- 10.91	95	96.8	329.6 +/- 11.1
			1100	0.3	0.095 +/- 0.0101	0.896 +/- 0.105	9.4 +/- 1.454	122 +/- 21.3	10.68 +/- 1.9	76	3.2	
RDY-090-QZH	a	0.1438	400	0.3	0.6949 +/- 0.0129	55.453 +/- 1.504	79.005 +/- 1.467	196.4 +/- 4.1	368.79 +/- 9.88	96	85.0	433.8 +/- 10.3
			700	0.3	0.4469 +/- 0.0098	10.051 +/- 0.426	22.315 +/- 0.793	124.6 +/- 4	60.36 +/- 2.8	86	13.9	
			1100	0.3	0.1046 +/- 0.0064	0.979 +/- 0.11	9.279 +/- 1.152	78.8 +/- 12.8	4.67 +/- 0.78	69	1.1	
RDY-091-QZH	a	0.1435	400	0.3	0.3522 +/- 0.0114	51.929 +/- 1.426	146.191 +/- 4.763	260.2 +/- 9.6	356 +/- 9.98	98	89.3	398.8 +/- 10.1
			700	0.3	0.2465 +/- 0.0073	6.849 +/- 0.256	27.542 +/- 0.992	126 +/- 6.8	42.81 +/- 1.8	90	10.7	
			1100	0.3	0.0076 +/- 0.0154	-0.036 +/- 0.097	-4.659 +/- 15.744	300.3 +/- 629.8	-			
RDY-092-QZH	a	0.1489	400	0.3	0.3248 +/- 0.0154	38.256 +/- 1.205	116.885 +/- 5.866	235.9 +/- 12.1	251.35 +/- 8.13	98	94.7	265.3 +/- 8.2
			700	0.3	0.0437 +/- 0.0115	2.202 +/- 0.157	49.981 +/- 13.563	193.8 +/- 60.8	13.97 +/- 1.08	94	5.3	
			1100	0.3	0.0136 +/- 0.0105	0.067 +/- 0.093	4.886 +/- 7.767	175.3 +/- 165.1	-			
RDY-093-QZH	a	0.1374	400	0.3	0.2753 +/- 0.0144	47.933 +/- 1.407	172.834 +/- 9.248	322.4 +/- 17.8	344.18 +/- 10.28	99	84.2	408.9 +/- 10.6
			700	0.3	0.1556 +/- 0.0139	9.319 +/- 0.327	59.432 +/- 5.489	202.1 +/- 20.3	64.71 +/- 2.41	95	15.8	
			1100	0.3	-0.0244 +/- 0.0101	0.123 +/- 0.09	-4.993 +/- 4.196	-163.3 +/- 83.2	-			

RDY-094-QZH	a	0.1256	400	0.3	0.1776 +/- 0.0133	34.568 +/- 1.037	193.216 +/- 14.658	349.1 +/- 27.7	271.96 +/- 8.29	99	89.3	304.5 +/- 8.5
			700	0.3	0.0705 +/- 0.013	4.275 +/- 0.221	60.199 +/- 11.427	171 +/- 36.5	32.49 +/- 1.79	95	10.7	
			1100	0.3	0.0135 +/- 0.0123	-0.06 +/- 0.097	-4.425 +/- 8.191	95.4 +/- 128.7	-			
RDY-095-QZH	a	0.1284	400	0.3	0.303 +/- 0.0153	39.979 +/- 1.14	131.03 +/- 6.708	257.8 +/- 14.3	305.42 +/- 8.92	98	92.1	331.6 +/- 9.0
			700	0.3	0.1208 +/- 0.0142	3.707 +/- 0.188	30.456 +/- 3.811	129.8 +/- 19.3	26.17 +/- 1.5	91	7.9	
			1100	0.3	0.0476 +/- 0.0146	-0.151 +/- 0.097	-3.168 +/- 2.241	50.7 +/- 30	-			
RDY-096-QZH	a	0.1478	400	0.3	0.3508 +/- 0.013	37.483 +/- 1.016	106.658 +/- 3.918	229.6 +/- 9.9	247.55 +/- 6.91	98	93.9	263.7 +/- 7.0
			700	0.3	0.0454 +/- 0.0109	2.507 +/- 0.147	55.176 +/- 13.545	270.7 +/- 72.6	16.11 +/- 1.02	95	6.1	
			1100	0.3	0.0087 +/- 0.0121	0.089 +/- 0.084	10.336 +/- 17.414	-27.6 +/- 171.7	-			

Notes:

[1] Computed by comparison to ^{20}Ne signal in air pipettes. 1-sigma uncertainty includes measurement uncertainty of ^{20}Ne signal in this analysis and the reproducibility of the air pipette signal (0.8%)

[2] Computed by comparison to ^{21}Ne signal in air pipettes. 1-sigma uncertainty includes measurement uncertainty of ^{21}Ne signal in this analysis and the reproducibility of the air pipette signal (2%)

[3] Isotope ratio measured internally during each analysis: does not involve normalization to the Ne isotope signals in the air pipettes.

[4] Analyses where excess ^{21}Ne was not distinguishable from zero at 1 sigma are not shown. Excess ^{21}Ne concentrations were calculated by normalization to either the ^{20}Ne or ^{21}Ne signal in the air pipettes, depending on which method yielded better precision.